Effect of low-permeability layers on spatial patterns of hyporheic exchange and groundwater upwelling

Gomez-Velez, Jesus D.; Krause, Stefan; Wilson, John L.

DOI:
10.1002/2013WR015054

AGU PUBLICATIONS

Water Resources Research

RESEARCH ARTICLE

10.1002/2013WR015054

Key Points:
- Low-permeability layers show long residence times and solute accumulation
- Low-permeability layers induce hydrodynamic sequestration
- Interface of low-permeability layer has the potential to be a biogeochemical hot spot

Supporting Information:
- Auxiliary Materials

Correspondence to:
J. D. Gomez-Velez,
jgomezvelez@usgs.gov

Citation:
Gomez-Velez, J. D., S. Krause, and J. L. Wilson (2014), Effect of low-permeability layers on spatial patterns of hyporheic exchange and groundwater upwelling, *Water Resour. Res.*, *50*, 5196–5215, doi:10.1002/2013WR015054.

Received 14 NOV 2013
Accepted 6 JUN 2014
Accepted article online 10 JUN 2014
Published online 27 JUN 2014

Effect of low-permeability layers on spatial patterns of hyporheic exchange and groundwater upwelling

Jesus D. Gomez-Velez[1,3], Stefan Krause[2], and John L. Wilson[1]

[1]Earth and Environmental Science Department, New Mexico Institute of Mining and Technology, Socorro, New Mexico, USA, [2]School of Geographical, Earth and Environmental Sciences, University of Birmingham, Birmingham, UK, [3]Now at U.S. Geological Survey, Reston, Virginia, USA

Abstract Bed form-induced hyporheic interactions are characterized by a nested system of flow paths that continuously exchange water, solutes, momentum, and energy. At the local scale, sediment heterogeneity plays a key role in the hydrodynamics and potential for biogeochemical transformations within the hyporheic zone. This manuscript explores the role of low-permeability sedimentary layers on the interplay between bed form-induced hyporheic exchange and groundwater upwelling. A hydrodynamic conceptualization that sequentially couples fully-turbulent flow in the water column and Darcian flow in the sediment is used. Low-permeability layers are characterized by long residence times and solute accumulation. Furthermore, these layers induce hydrodynamic sequestration due to the relocation and, in some cases, emergence of new stagnation zones. Spatial patterns of residence time distributions and flushing intensities indicate that the interface of the low-permeability layers has the potential to be a hot spot for biogeochemical transformations and flow acceleration near such interface can increase the mobilization capacity for the products of redox chemical and microbial processes. A discussion about the possible implications that hydrodynamic changes have on the biogeochemistry of hyporheic zones is presented; however, further biogeochemical experimentation and modeling are needed to validate these arguments.

1. Introduction

Exchange fluxes across the aquifer-river interface not only connect groundwater and surface water resources and thus affect stream hydraulics and groundwater flow, but they also significantly impact temperature patterns and dynamics [*Cardenas and Wilson*, 2007a; *Arrigoni et al*., 2008; *Acuña and Tockner*, 2009], biogeochemical cycling [*Battin et al*., 2008; *Gu et al*., 2007, 2008; *Krause et al*., 2009, 2013], and ecological functioning [*Burkholder et al*., 2008; *Brunke and Gonser*, 1997; *Hayashi and Rosenberry*, 2001; *Boulton and Hancock*, 2006; *Krause et al*., 2011a] of the stream-aquifer continuum, that is, the hyporheic zone. Understanding hyporheic-process dynamics requires a detailed knowledge of the major drivers (e.g., spatial variability of head at the sediment-water interface (SWI) and hydraulic conductivity) and controls (e.g., groundwater upwelling) of hyporheic exchange fluxes (HEF) and their characteristic spatial scales, patterns, and temporal dynamics [*Fanelli and Lautz*, 2008; *O'Connor and Harvey*, 2008]. In this regard, the spatial extent of the hyporheic mixing zone and the range and character of hyporheic residence time distributions become fundamental metrics to evaluate the physical, biological, and biogeochemical role of hyporheic exchange at the local, reach, and watershed scale [*Zarnetske et al*., 2011a; *Gomez et al*., 2012].

1.1. Hyporheic Exchange, Heterogeneity, and Groundwater Upwelling: Empirical Evidence

Interactions between channel flow and river morphology induce head variations that drive hyporheic exchange along the river corridor [*Buffington and Tonina*, 2009]. The nature of these interactions has been studied with field observations and laboratory experiments in meanders [*Kasahara and Hill*, 2007], riffle-pool sequences [*Storey et al*., 2003; *Kasahara and Wondzell*, 2003; *Kaser et al*., 2009; *Tonina and Buffington*, 2007, 2011], step-pool sequences [*Kasahara and Wondzell*, 2003; *Hassan et al*., 2014], dunes and ripples [*Thibodeaux and Boyle*, 1987; *Elliott and Brooks*, 1997; *Bhaskar et al*., 2012; *Fox et al*., 2014], debris [*Sawyer et al*., 2011, 2012], and restoration structures [*Fanelli and Lautz*, 2008; *Crispell and Endreny*, 2009; *Endreny et al*., 2011; *Briggs et al*., 2012], among others. In all cases, the presence of multiple scales of interaction, involving nested systems of flow paths with varying lengths, velocities, and residence times (RT) and stagnation zones is a fundamental and ubiquitous hydrodynamic feature of the exchange process (see Figure 1) [see *Wörman et al*., 2007; *Cardenas*, 2008; *Stonedahl et al*., 2010; *Gomez and Wilson*, 2013].

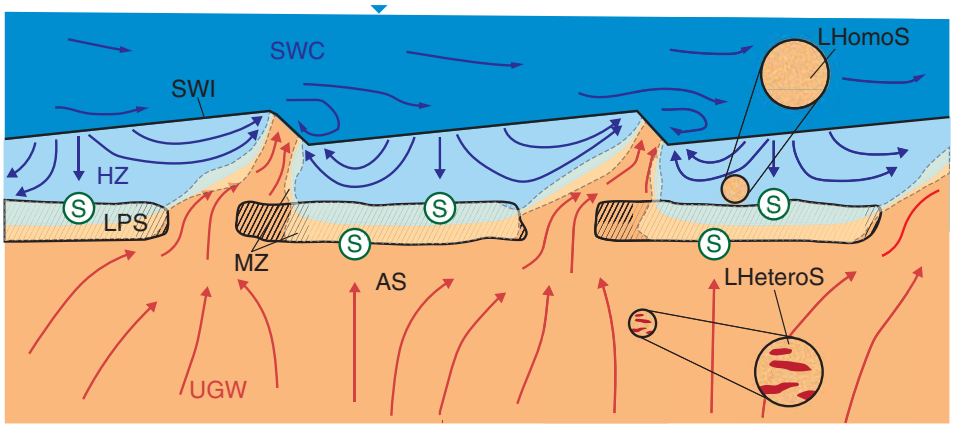

SWI = sediment-water interface, LPS= low-permeability sediments, S = stagnation zones, AS = ambient sediment
SWC = stream water column, UGW = upwelling groundwater, HZ = hyporheic zone, MZ = mixing zone,
LHomoS = locally homogeneous aquifer, LHeteroS = locally heterogeneous sediment

Figure 1. Schematic representation of the role of low-permeability sedimentary layers on the interplay between bed form-induced hyporheic exchange and groundwater upwelling. Turbulent flow in the stream water column (SWC) induces spatial head variations along the sediment-water interface (SWI), which, at the same time, drives exchange with the hyporheic zone (HZ). The extent of the HZ is modulated by the upwelling groundwater (UGW) and the presence of low-permeability sediments (LPS), resulting in stagnation zones (S) above and bellow the LPS. Diffusion and mechanical dispersion mix hyporheic and upwelling waters along the HZ's interface (dashed lines). The thickness of this mixing zone (MZ) depends on the relative role of advection, diffusion, and dispersion. Typically, diffusion dominates within the LPS, resulting in a MZ that expands over the low-permeability layer. On the other hand, as we move away from the LPS, the thickness of the MZ initially increases due to mechanical dispersion, but eventually succumbs to converging flow and advective transport near the SWI. The inserts magnify examples of locally homogeneous sediment (LHomoS) and locally heterogeneous sediment (LHeteroS), where the scale of heterogeneity is much smaller than the scale of the LPS or the bed forms.

Sediment heterogeneity is an additional driver of hyporheic exchange and a modulator for groundwater upwelling [*Tonina and Buffington*, 2009]. Field observations highlight the importance of this mechanism and its characteristic length scales in the hydrodynamics of the HZ and stream biogeochemical cycling. For example, *Cardenas et al*. [2004] used field measurements of hydraulic conductivity and kriging to reconstruct heterogeneous fields of hydraulic conductivity in a sandbed channel. This study found that spatial changes in hydraulic conductivity can induce important changes in the HEF and RT. In particular, the impact of heterogeneity relative to other controlling factors depends on the relative positions of the heterogeneities and the geomorphic features. Observations in lowland rivers have also shown that structural heterogeneities (i.e., heterogeneities with characteristic length scales of the order of the geomorphic features driving exchange or longer; see LPS in Figure 1) can substantially impact exchange flow patterns between groundwater and surface water and the spatial distribution of solutes such as nitrogen and oxygen within the sediments [*Krause et al*., 2011b, 2012a; *Angermann et al*., 2012; *Krause et al*., 2013].

In a controlled environment, flume experiments have been used to understand the hydrodynamics of hyporheic exchange in the presence of heterogeneities. Experiments in heterogeneous sediment beds with small-scale correlation lengths [*Salehin et al*., 2004] and stratified sediments [*Packman et al*., 2006; *Marion et al*., 2008], a particular case of structural heterogeneity, have shown that spatial variability in hydraulic properties significantly impact the hyporheic zone, favoring horizontal transport, limiting vertical penetration of the hyporheic zone, and, in some cases, inducing higher exchange fluxes and shorter residence times. Figure 1 illustrates both locally heterogeneous sediment with small-scale correlations lengths (see close-up of LHeteroS) and structural heterogeneities (see LPS).

Superimposed on the driving forces of spatial variability in head and hydraulic conductivity is the effect of groundwater upwelling (red arrows in Figure 1) from large-scale groundwater flow paths [*Sophocleous*, 2002]. Even though isolating the individual effects of competing drivers and controls is challenging, some detailed empirical studies have studied the modulating effect of groundwater upwelling in the hydrodynamics and extent of the hyporheic zone [see, for example, *Krause et al*., 2011b; *Angermann et al*., 2012; *Bhaskar et al*., 2012; *Fox et al*., 2014]. Notice, however, that with the exception of the field observations of *Krause et al*. [2011b, 2012a], *Angermann et al*. [2012], and *Krause et al*. [2013], the interplay between groundwater upwelling and heterogeneity has been ignored in previous observational and experimental studies. This is particularly important to explain the significant spatial variability of groundwater upwelling observed in lowland rivers, which is commonly attributed only to spatial variations of streambed conductivity

[*Genereux et al*., 2008; *Rosenberry and Pitlick*, 2009; *Leek et al*., 2009; *Kennedy et al*., 2009a, 2009b; *Krause et al*., 2012a, 2013; *Naranjo et al*., 2013].

1.2. The Role of Mathematical Models

Model-based quantifications of HEF are necessary to gain mechanistic understanding, and therefore critical to consolidate observations, guide experimental design, and upscale processes at the reach and watershed scales [e.g., *Munz et al*., 2011; *Endreny and Lautz*, 2012; *Krause et al*., 2012b; *Gomez et al*., 2012]. Simplified model domains representing periodic triangular bed forms, dunes, and ripples of variable wavelengths, or even flat porous streambeds, have significantly improved our understanding of the impacts of advective pumping due to steady and unsteady turbulent flows in homogeneous sediments [*Cardenas and Wilson*, 2007b; *Boano et al*., 2007, 2011], including the impact of groundwater upwelling [e.g., *Cardenas and Wilson*, 2006, 2007c; *Boano et al*., 2008, 2009]. Modeled upwelling reduces the depth and extent of the hyporheic zone, supporting experimental evidence from field and laboratory studies [*Bhaskar et al*., 2012; *Fox et al*., 2014], and results in nonuniform upwelling zones at the sediment-water interface (Figure 1) [see, for example, *Cardenas and Wilson*, 2006, Figure 2]. This is consistent with the variability of groundwater upwelling observed in lowland rivers. The role of upwelling on hyporheic zone residence time distributions for homogeneous sediments has not yet been explored [for example, *Cardenas and Wilson*, 2006, excludes upwelling].

Mathematical models have been used to consolidate the observations of *Salehin et al*. [2004], *Packman et al*. [2006], and *Marion et al*. [2008] in stratified and heterogeneous bed sediments. *Tonina and Buffington* [2011] explored the role that stratification, represented by a depth-varying impervious layer, has on hyporheic exchange in riffle-pool sequences. Imposing an impervious layer effectively decreases the domain available for exchange, truncating flow paths and residence times; however, the lack of exchange with this impervious layer ignores the effects that a more realistic pervious layer would have on the flow field, residence times, and sequestration within the hyporheic zone (notice that typical flumes have a solid bottom, which implicitly mimics the effect of an impervious layer). Some previous modeling studies have included small-scale heterogeneity implicitly [e.g., *Cardenas et al*., 2008; *Janssen et al*., 2012; *Bardini et al*., 2012] with the use of a dispersion coefficient (accounts for spatial velocity fluctuations that are not modeled explicitly) or explicitly using stationary random fields with spatial correlations that are small when compared to the size of the domain [e.g., *Sawyer and Cardenas*, 2009; *Bardini et al*., 2013]. In particular, the few modeling studies that have explicitly considered horizontal variability in subsurface hydraulic conductivity assumed no-flow conditions across the lower model boundary, thus excluding the impact of upwelling groundwater [e.g., *Cardenas et al*., 2004; *Sawyer and Cardenas*, 2009; *Ward et al*., 2011, 2012; *Bardini et al*., 2013].

1.3. Main Propose of This Study

This manuscript explores the role of low-permeability sedimentary layers on the interplay between bed form-induced hyporheic exchange and groundwater upwelling. Our model conceptualization is inspired by field observations in lowland rivers where low-permeability layers, typically composed of peat and silt deposits, constrain the amount of hyporheic exchange and are associated with spatial variability in groundwater upwelling [*Krause et al*., 2011b, 2012a; *Angermann et al*., 2012; *Krause et al*., 2013]. Heterogeneities at the scale of the geomorphic features driving hyporheic exchange, or longer, are included in the model. These, in turn, induce important changes on the spatial variability of groundwater upwelling. Fluxes, exchange patterns, spatial extent of hyporheic zones, and hyporheic residence time distributions are the metrics used in the analysis. In particular, we focus on exchange driven by pressure gradients due to streamflow over dunes; however, the results are presented in a dimensionless framework, and as long as geometrical similarity is maintained, the conclusions drawn can be extended to other geomorphic features driven by slightly different pressure distributions at the sediment-water interface but characterized by similar nested scales of interaction (e.g., ripples, rifle-pool sequences, step-pool sequences, and logs). Finally, while not the focus of this paper, an important motivation is to understand the influence of heterogeneities on biogeochemical cycling and stream ecology. We briefly explore these implications at the end of the manuscript.

2. Methods

2.1. Conceptual Model Description

A simple two-dimensional conceptualization is used to explore the interplay between bed form-induced hyporheic exchange, groundwater upwelling, and large-scale heterogeneities (i.e., heterogeneities with a

characteristic length scale of the order of the bed form length or larger). The domain is composed of the water column and sediment subdomains (see Figure 2), which are sequentially coupled at the sediment-water interface (SWI) ($\partial\Omega_{SWI}$) and which have a prescribed spatially periodic pressure for the upstream ($\partial\Omega_u$) and downstream ($\partial\Omega_d$) boundaries ($x = -L$ and $x = 2L$). Modeling three dunes with a periodic boundary condition (PBC) allows us to mimic a large dune-bed configuration with a finite domain and avoid numerical instabilities due to boundary effects by focusing the analyses on the center bed form ($x \in [0, L]$). The upper boundary of the domain corresponds to the top of the water column subsystem ($\partial\Omega_t$), located at $y = d$, and the lower boundary of the domain corresponds to the bottom of the sediment subdomain ($\partial\Omega_b$), located at $y = -d_{gw}$.

The SWI caps an asymmetric dune with total length L, crest length L_c, and crest height H. The sediment subdomain is composed of two homogeneous and isotropic materials with contrasting physical properties: sand or sand-and-gravel dominated streambed sediment and horizontal zones of low permeability (e.g., clay, silt, or peat). We refer to the former material as the *ambient sediment* and the latter as the *low-permeability sediment* throughout the manuscript. The geometry and location for the low-permeability layer shown in Figure 2 are given by the thickness w, depth from the surface d_l, and the horizontal extent parameters s and r. Notice that the location and geometry of this layer can be described by 4 degrees of freedom. In this manuscript, we focus on two illustrative cases commonly found in natural systems [e.g., *Conant*, 2004; *Genereux et al*., 2008; *Kennedy et al*., 2009a, 2009b; *Rosenberry and Pitlick*, 2009; *Krause et al*., 2013; *Naranjo et al*., 2013]: (i) a continuous low-permeability layer, i.e., $s = 0$ (continuous scenarios) and (ii) a discontinuous layer with a constant opening or window at different horizontal locations (funneling scenarios).

The physical properties of the porous media are given by the intrinsic permeability k_i, effective porosity θ_i, and longitudinal and transversal dispersivities α_{Li} and α_{Ti}, respectively. The subscript i is 0 and l for the ambient sediment and low-permeability layer, respectively. The ratio of the intrinsic permeabilities, $k_r = k_l/k_0$, is varied over several orders of magnitude to evaluate the sensitivity of the system's hydrodispersive characteristics. The ratio $k_r = 1$ corresponds to the homogenous case, that is, to the absence of a low-permeability layer. To maintain consistent and physically based orders of magnitude for the other physical properties of the porous media, we use well-known empirical relationships between hydraulic conductivity, porosity, and dispersivities to relate values of k_r with similar ratios of porosity and longitudinal dispersivity. Combining a simple relationship between the grain-size distribution and permeability ($k \propto d_m^2$) and the Kozeny-Carman equation ($k \propto \theta^3/(1-\theta)^2$) [*Freeze and Cherry*, 1979; *Domenico and Schwartz*, 1990; *Koltermann and Gorelick*, 1995; *Brayshaw et al*., 1996], where d_m is mean grain size and θ is effective porosity, for both the ambient sediment and the low-permeability layer, a third-order polynomial that relates $\theta_r = \theta_l/\theta_0$ and θ_0 can be

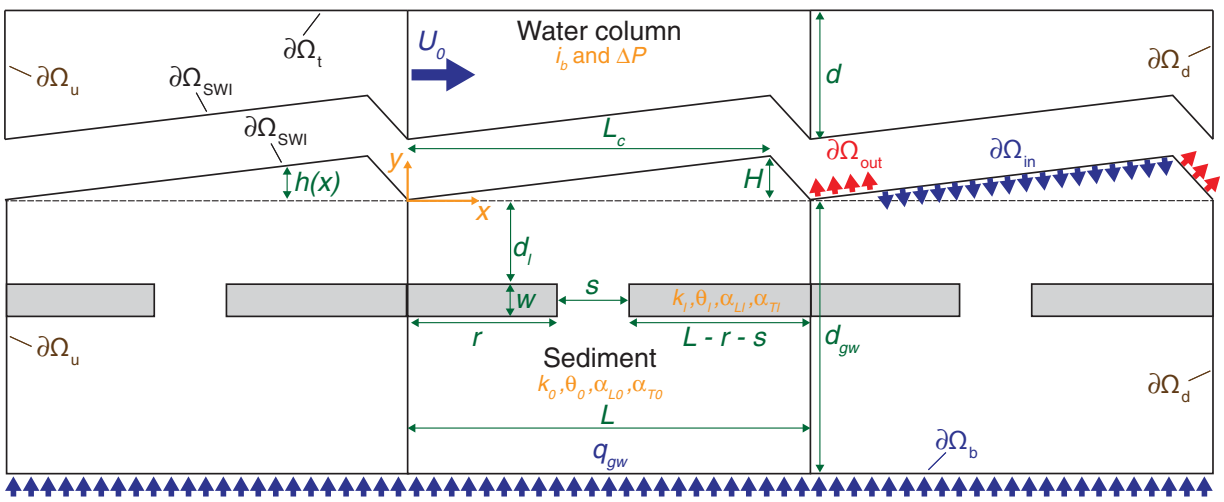

Figure 2. Schematic representation of the two-dimensional alluvial system: (top) water column and (bottom) sediment. The domain used for the mathematical model assumes that the asymmetrical dunes repeat periodically downstream (i.e., periodic boundary condition in boundaries $\partial\Omega_u$ and $\partial\Omega_d$). Turbulent flow in the water column is simulated with the steady state Reynolds-averaged Navier-Stokes (RANS) equations, and the resulting pressure distribution at the sediment-water interface ($\partial\Omega_{SWI}$) is prescribed as a Dirichlet boundary driving flow within the sediment. This forcing results in spatially distributed inflow ($\partial\Omega_{in}$) and outflow ($\partial\Omega_{out}$) boundaries at $\partial\Omega_{SWI}$. Uniform groundwater upwelling is prescribed along the boundary $\partial\Omega_b$.

obtained. $\theta_r = 1$ is the only real root of this polynomial for $\theta_0 < 0.75$, so this value is used for all simulations (i.e., $\theta_l = \theta_0$). For dispersivity, empirical relationships between the grain-size distribution and dispersivity ($\alpha_L \propto d_m$) [e.g., *Xu and Eckstein*, 1997] are used. In this case, $\alpha_{Lr} = \alpha_{Ll}/\alpha_{L0} \propto \sqrt{k_r}$, which is consistent with observations in unconsolidated materials [*Harleman et al.*, 1963; *Dullien*, 1991]. To summarize, the following relationships are used to relate the ratios of the physical properties of the porous media in the ambient sediment and low-permeability layers:

$$k_r = \frac{k_l}{k_0}, \theta_r = \frac{\theta_l}{\theta_0} = 1, \text{and } \alpha_{Lr} = \frac{\alpha_{Ll}}{\alpha_{L0}} = \sqrt{k_r} \tag{1}$$

The ratio of the longitudinal and transverse dispersivity is assumed constant, $\alpha_{Tl}/\alpha_{Ll} = 0.1$ [*Gelhar et al.*, 1992]. It is important to notice that these empirical relationships, even though commonly used and well known, are useful to obtain a first-order approximation; however, their validity is restricted to the limited data sets used and involve coefficients that can vary considerably and affect the proposed relationships. Additionally, the importance of α_{Lr} vanishes as k_r decreases, since the low-permeability layer becomes diffusion dominated and mechanical dispersion within the layer becomes negligible.

2.2. Flow Model

Subcritical streamflow with a uniform water depth d and mean downstream velocity U_0 is assumed for the water column subdomain. Turbulent flow in the water column is simulated with the steady state Reynolds-averaged Navier-Stokes (RANS) equations and the $k - \omega$ closure scheme. The resulting normalized pressure distribution along the SWI, and thus the pattern of hyporheic flow, is essentially the same for fully turbulent flow across the range of Reynolds numbers explored (see section 1 in supporting information and *Cardenas and Wilson* [2007d]). Hyporheic flow in the sediment subdomain is described by Darcy's law and the groundwater flow equation for steady flow. The models, boundary conditions, and coupling of subdomains (see section 1 in supporting information) are similar to those presented in *Cardenas and Wilson* [2007d, 2007c].

2.3. Residence Time Model

For a representative elementary volume (REV) centered at a location $\mathbf{x}$, the residence time distribution (RTD) $f(\mathbf{x}, \tau)$ [T^{-1}], a probability density function, represents the proportion of fluid parcels within the REV with a residence time (RT) τ ($\tau \geq 0$). Then, the product $f(\mathbf{x}, \xi)\,\mathrm{d}\xi$ is the probability of finding water particles with a RT within the interval $[\xi, \xi + \mathrm{d}\xi]$ at the location $\mathbf{x}$. The cumulative residence time distribution, CRTD or $F(\mathbf{x}, \tau)$, represents the contribution of particles younger than τ and is defined as:

$$F(\mathbf{x}, \tau) = \int_0^{\tau} f(\mathbf{x}, \xi)\mathrm{d}\xi \tag{2}$$

Numerically, solving for the CRTD is an easier and more stable problem, since the boundary and initial conditions are easier to handle. The moments of the RTD are an important metric defined as

$$a_n(\mathbf{x}) = \int_0^{\infty} \xi^n f(\mathbf{x}, \xi)\mathrm{d}\xi \tag{3}$$

where $n = 1, 2, \ldots$, and $a_0(\mathbf{x}, t) = 1$. They are related to the standard central moments with the following relationships:

$$\mu_\tau = \mathrm{E}[\tau] = a_1 \tag{4}$$

$$\sigma_\tau = \sqrt{\mathrm{Var}[\tau]} = \sqrt{a_2 - \mu_\tau^2} \tag{5}$$

where μ_τ and σ_τ are the mean and standard deviation of the RTD, respectively.

Focusing on the sediment subdomain we model the moments and CRTD, and then estimate the RTD as $f(\mathbf{x}, \tau) = \partial F(\mathbf{x}, \tau)/\partial\tau$ using the methods presented in *Gomez and Wilson* [2013]. The appropriate RT boundary for steady hyporheic flow field are presented for the first time in Appendix A. The bottom boundary condition accounts for upwelling groundwater.

The RTD boundary condition for upwelling groundwater, f_{gw}, is in principle unknown. To address this issue, we explored Neumann and Dirichlet boundary conditions. First, the Neumann condition assumes a zero-gradient RTD at the boundary ($\mathbf{n} \cdot \nabla f = 0$ over $\partial\Omega_b$), resulting in a cleaner mathematical statement without the need for a functional form of f_{gw}; however, the solution always converges to extremely old waters and truncates contributions from young waters (not shown), which is contrary to observations. On the other hand, a Dirichlet condition, which is used in this analysis, specifies a functional form for f_{gw}. Multiple functional forms have been proposed for the RTD of groundwater discharging to streams (see *McGuire and McDonnell* [2006], for a review). The exponential RTD is simple (only one parameter) and by far the most commonly used model in hydrological applications with mean residence times commonly found within the interval 1–10 years [*McGuire and McDonnell*, 2006]. The exponential RTD with mean $\mu_{\tau,gw}$ and standard deviation $\sigma_{\tau,gw} = \mu_{\tau,gw}$ is given by

$$f_{gw}(\tau) = \frac{1}{\mu_{\tau,gw}} \exp\left(-\frac{\tau}{\mu_{\tau,gw}}\right) \tag{6}$$

where the central moments are related to the moments as $a_{1,gw} = \mu_{\tau,gw}$ and $a_{2,gw} = \sigma^2_{\tau,gw} + \mu^2_{\tau,gw} = 2\mu^2_{\tau,gw}$. Without loss of generality, we assumed $a_{1,gw} = \mu_{\tau,gw} = 1$ year in our simulations. Notice, however, that this RTD can have components that vary over orders of magnitude, typically going from years [*McGuire and McDonnell*, 2006] to decades [*Kennedy et al.*, 2009b] and even centuries or longer [*Frisbee et al.*, 2011, 2013] with the presence of multimodality [*Corcho-Alvarado et al.*, 2007; *Gomez and Wilson*, 2013]. Since the longer time scales of this distribution have a minimal impact on the hyporheic zone's much younger RTD (mostly due to mixing at the HZ interface with the upwelling groundwater), the use of an exponential model is justified.

Table 1. Values Explored in the Analysis

Variable	Definition	Values
Turbulent Water Column		
U		0.30 m s^{-1}
d		0.5 m
$\Delta P/L$		0.7 Pa m^{-1}
i_b		1.5×10^{-4}
Sediment Geometry		
L		1 m
H^*	H/L	0.075
L_c^*	L_c/L	0.9
d_{gw}^*	d_{gw}/L	1.5
d_l^*	d_l/L	0.05, 0.15, 0.25, 0.35, 0.45, 0.60, 0.80, and 1
w^*	w/L	0.1
r^*	r/L	For continuous 1 and for funneling 0, 0.2, 0.4, 0.6, and 0.8
s^*	s/L	For continuous 0 and for funneling 0.2
Sediment Properties		
θ_0		0.4
k_0		10^{-10} m^2
θ_r	θ_l/θ_0	1
k_r	k_l/k_0	1, 10^{-1}, 10^{-2}, 10^{-3}, 10^{-4}, and 10^{-5}
α_L^*	α_L/L	3×10^{-3}
α_T^*	α_T/L	0.1 α_L^*
ε		0.75
Fluid Properties		
ρ		998.2 kg m^{-3} (at 20°C)
μ		1.002×10^{-3} Pa s (at 20°C)
D_m		10^{-9} m^2 s^{-1} (at 20°C)
g		9.81 m s^{-2}
Groundwater Upwelling		
q_{gw}^*	q_{gw}/q_c	0, 0.142, 0.711, 1.42, 7.11, and 14.2
$\mu_{\tau,gw}^*$	$\mu_{\tau,gw}/t_c$	5.5078
$\sigma_{\tau,gw}^*$	$\sigma_{\tau,gw}/t_c$	5.5078
Characteristic Scales		
l_c	L	1 m
t_c	$(\theta_0 L)/q_c$	5.7257×10^6 s
q_c	$(k_0/\mu)(\triangle P/L)$	6.9860×10^{-8} m s^{-1}

2.4. Definition of the Hyporheic Zone

The hyporheic zone (HZ) is defined in this paper as the area within the sediment with more than 50% stream water. This geochemical definition is similar to the one proposed by *Triska et al.* [1989], who uses 10%, but has the advantage of resulting in a HZ similar to the one obtained with a hydrodynamic definition of the HZ [*Gooseff*, 2010] and it is less sensitive to the dispersivity values selected. Additionally, we focus on the local HZ, corresponding to the center bed form in the interval $x \in [0, L]$. Notice, however, that the periodic nature of the domain and flow field results in a local HZ that repeats for each bed form. The steady state spatial distribution of a conservative solute within the sediments, that originates from the stream above the center bed form (concentration $C = 1$), is given by a solution of the advective-dispersion equation with appropriate boundary conditions (see section 2 in supporting information). The local HZ corresponds to the area with concentration $C(\mathbf{x}, t) \geq 0.5$, as illustrated in Figure 3 below.

2.5. Characteristic Scales, Nondimensionalization, and Scenarios

The following characteristic scales are used to nondimensionalize the model (see section 3 in

supporting information) and to assist the discussion

$$\text{Length}: \quad l_c = L; \text{Time}: \quad t_c = \frac{\theta_0 L}{q_c}; \text{Flux}: \quad q_c = \frac{k_0}{\mu}\frac{\triangle P}{L} \tag{7}$$

where g is acceleration of gravity $[LT^{-2}]$, ρ is fluid density $[ML^{-3}]$, μ is fluid dynamic viscosity $[ML^{-1}T^{-1}]$, and $\Delta P = \rho g i_b L$ is the pressure drop at the SWI caused by flow over one dune in a channel with average slope i_b $[ML^{-1}T^{-2}]$. Table 1 presents the variables explored in the analysis.

3. Results and Discussion

Simulations were performed with COMSOL Multiphysics. The mesh used for the turbulent flow subdomain has about 63,000 elements with refinement along the SWI boundary. The sediment subdomain has about 115,000 elements with telescopic refinement close to the surface and within the low-permeability layer. Finite element size was chosen to maintain numerical Peclet numbers below one in both advection and diffusion dominated zones, minimizing artificial oscillations or other numerical instabilities [*Huyakorn and Pinder*, 1983]. Finally, in both subdomains, the solutions are mesh independent.

3.1. Hyporheic Flow Patterns

The turbulent streamflow-generated pressure distribution along the SWI drives two hyporheic flow circulation systems with different sizes and penetration; the smaller one flowing to the upstream end of the dune's stoss and the larger one flowing toward the downstream end (see diverging flow vectors in Figure 3). These circulation systems are present under both neutral (no upwelling) and upwelling conditions (Figures 3a and 3d) and, as shown later in this manuscript, strongly impact the RTD at the outlet of the HZ. A fundamental feature of these flow fields is the presence of stagnation zones, which for the homogeneous cases become shallower and move from left to right as groundwater upwelling increases (Figures 3a and 3d). The presence of a low-permeability layer increases the flux intensities and compresses the main circulation systems relative to homogeneous conditions. If the depth of the low-permeability layer is small enough, or the upwelling flux large enough, then the HZ does not penetrate below the low-permeability layer (Figures 3b and 3f), or even reach as deep as the top of the low-permeability layer (Figure 3e) although the flow field is modified. An interesting feature is observed in Figure 3c, where a circulation cell appears in the window through a discontinuous low-permeability layer. Water circulates within the window, resulting in RTDs skewed toward younger residence times when compared to the case of continuous low-permeability zone ($s^* = 0$). This is similar to a transient storage zone; although as shown in section 3.3.2, it contributes relatively low amounts of mass to the outlet and therefore has a negligible contribution to the flux-weighted RTD. This feature of the window disappears with increasing upwelling (Figures 3f and 7f) and is less prevalent for larger values of k_r (with less of a contrast in permeability, e.g., $k_r = 10^{-1}$; not shown) and deeper low-permeability layers (not shown).

Introducing a low-permeability layer modifies stagnation-zone locations and, in some cases, new stagnation zones appear. Additionally, stagnation-zone locations are modulated by the magnitude and direction of the upwelling flow. The interplay between the ambient horizontal flow (driven by the horizontal pressure drop) and upwelling induces a net upwelling direction between the horizontal and vertical (see large arrows in Figures 3d–3f), affecting the bed form-induced HZ in different ways as upwelling intensity changes.

The horizontal location of discontinuities in the low-permeability layer (given by parameter r) affects the flow field, extent of the hyporheic zone, and residence times. Hydrodynamic changes depend on the location of the window relative to the two hyporheic flow circulation systems (HFCS) and the modulating role of groundwater flow. Under neutral groundwater conditions, a discontinuity induces a deeper and preferential penetration of the HZ (see Figures 3c, 6c, and 7c). This effect is amplified as the window's location approaches the deeper parts of the hyporheic flow circulation systems (i.e., locations where the flow systems penetrate deeper within the sediment). Under upwelling conditions, the funneling effect of the discontinuity contracts the HZ, leading to shorter RTs and dominance of shallower flow paths (see Figures 3f,

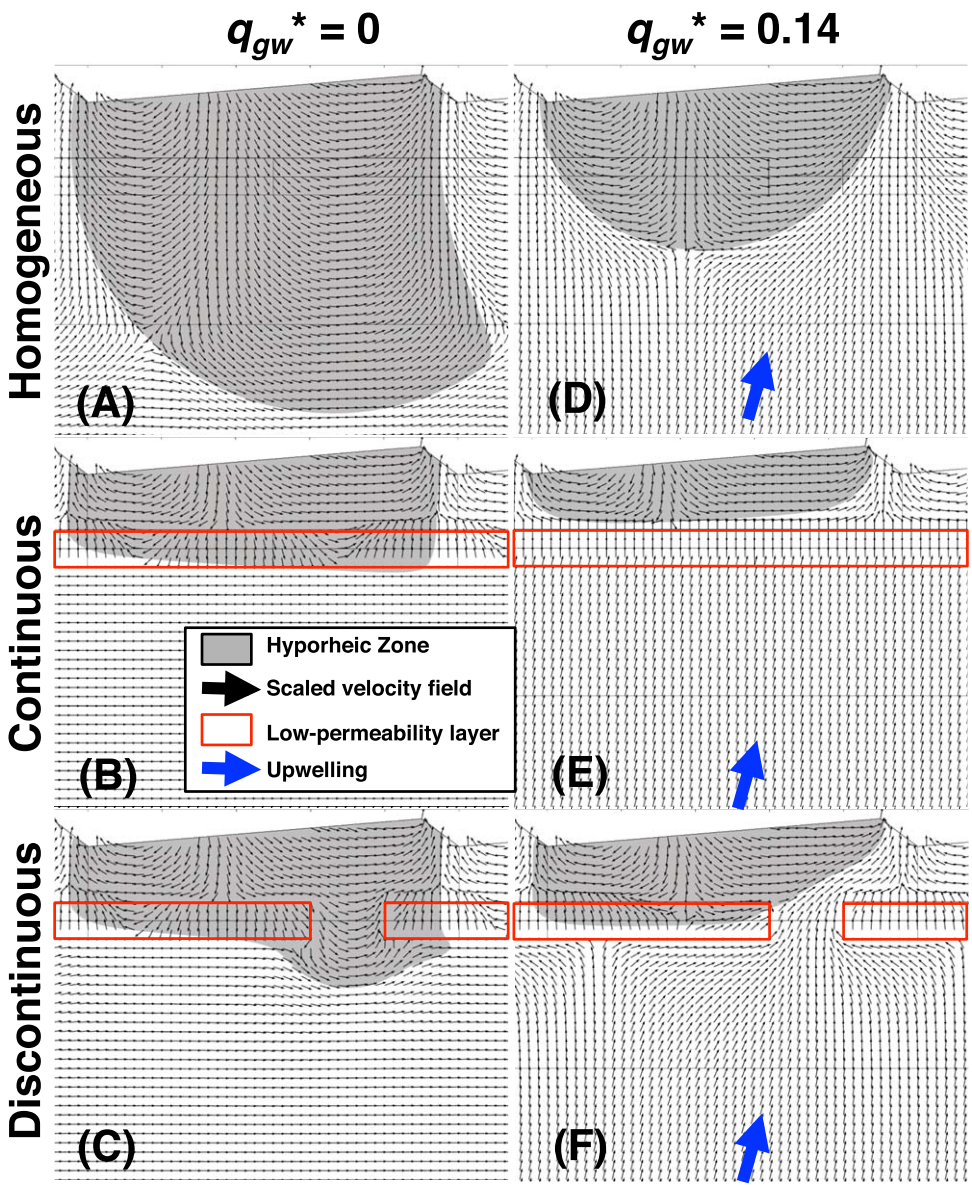

Figure 3. Examples of different flow fields (arrows) and HZs (gray surface) under neutral (left column; A-C) and upwelling (right column; D-F) conditions. From top to bottom, rows correspond to homogeneous ($k_r = 1$), continuous ($k_r = 10^{-5}$), and funneling ($k_r = 10^{-5}$, $s^* = 0.2$, and $r^* = 0.6$) scenarios. Low-permeability layer is diffusion controlled in all cases; however, the arrows within the layer are shown to illustrate flow direction. Upwelling scenarios use $q^*_{gw} = 1.42$ and other parameters are given in Table 1.

6d, and 7f). The resilience of the flow patterns, however, is larger when the window is closer to the regions where the hyporheic flow circulation systems are deeper (not shown).

3.2. Net Response of the HZ

The hyporheic zone discharges to the SWI and stream in the vicinity of the bed form's lee face. The location of this discharge zone is not sensitive to the presence of the low-permeability zone, whether continuous or discontinuous and whether neutral (Figures 3a–3c) or upwelling (Figures 3d–3f), unless the upwelling flux is excessive ($q^*_{gw} \geq 14$; not shown).

A sensitivity analysis was performed for the case of a continuous low-permeability layer ($s^* = 0.0$, see Figure 4 and Table 1 for the parameters used). Each column in Figure 4 corresponds to a different relative permeability, k_r, with $k_r = 1$ in the right-hand column corresponding to the homogeneous case without a low-permeability

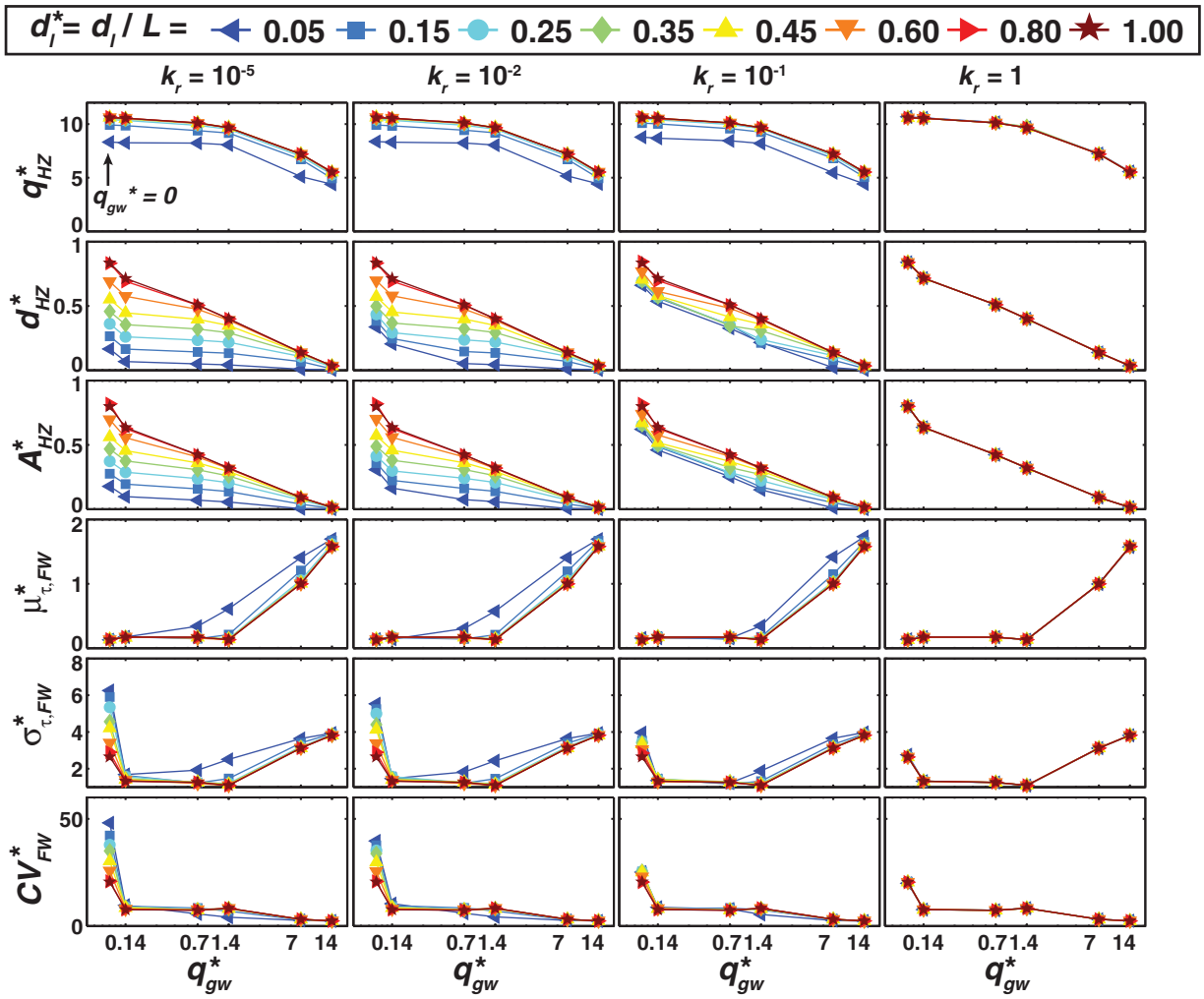

Figure 4. Sensitivity of the HEF metrics to changes in groundwater upwelling (q_{gw}^*; x axis) and depth of the continuous ($s^* = 0.0$) low-permeability layer (d_l^*; colors). Rows correspond to the dimensionless metrics: net hyporheic flux (q_{HZ}^*), maximum depth of the HZ (d_{HZ}^*), area of the HZ (A_{HZ}^*), flux-weighted mean RT ($\mu_{\tau,FW}^*$), flux-weighted standard deviation RT ($\sigma_{\tau,FW}^*$), and flux-weighted coefficient of variation ($CV_{FW}^* = \sigma_{\tau,FW}/\mu_{\tau,FW}$). Columns correspond to different values of the ratio k_r. Since the x axis is logarithmic in each subplot, the first set of symbols to the left represents the value of the metric under neutral conditions ($q_{gw}^* = 0$). See Table 1 for the values of the other parameters.

layer. Each row corresponds to a different dimensionless metric (see below) representing, from the top down, the hyporheic exchange flux (HEF), the maximum depth of the hyporheic zone, the area of the hyporheic zone (e.g., the gray areas in Figure 3), and the mean, standard deviation, and coefficient of variation of the hyporheic zone RTD. Each point represents a different flow field due to changes in the depth of the low-permeability layer, d_l/L (colors), and/or dimensionless strength of the upwelling groundwater, q_{gw}^* (x axis).

The HEF metric in the first row of Figure 4 corresponds to the flux-weighted values integrated along the sections of the SWI discharging hyporheic water to the stream. The hyporheic exchange flux is estimated as

$$q_{HZ} = \frac{\int_{\partial\Omega_{out,HZ}} \mathbf{n} \cdot \mathbf{q} \mathrm{d}\mathbf{x}}{\int_{\partial\Omega_{SWI}} \mathrm{d}\mathbf{x}} \tag{8}$$

were $\Omega_{out,HZ}$ is the outflow boundary discharging hyporheic water ($C > 0.5$) originating from the center dune. This flux is scaled by the characteristic flux value q_c (see equation (7) and Table 1) as $q_{HZ}^* = q_{HZ}/q_c$. The

area of the hyporheic zone and its penetration depth are scaled as $A^*_{HZ}=A_{HZ}/L^2$ and $d^*_{HZ}=d_{HZ}/L$, respectively. The flux-weighted value of ζ, where the scalar ζ represents either $f(\mathbf{x}, \tau)$, $F(\mathbf{x}, \tau)$, $\mu_\tau(\mathbf{x})$, or $\sigma_\tau(\mathbf{x})$, is defined as

$$\zeta_{FW}(\tau)=\frac{\int_{\partial\Omega_{out,HZ}}(\mathbf{n}\cdot\mathbf{q})\zeta(\mathbf{x},\tau)\mathrm{d}\mathbf{x}}{\int_{\partial\Omega_{out,HZ}}\mathbf{n}\cdot\mathbf{q}\mathrm{d}\mathbf{x}} \tag{9}$$

The characteristic time scale t_c (see equation (7) and Table 1) is used to scale residence times and the flux-weighted values as $\tau^*=\tau/t_c$, $f^*_{FW}=f_{FW}t_c$, $\mu^*_{\tau,FW}=\mu_{\tau,FW}/t_c$, and $\sigma^*_{\tau,FW}=\sigma_{\tau,FW}/t_c$. Finally, the coefficient of variation is estimated as $CV^*_{FW}=\sigma^*_{\tau,FW}/\mu^*_{\tau,FW}$.

3.2.1. Hyporheic Exchange Flux and Penetration

The net hyporheic exchange flux (HEF, q^*_{HZ}), penetration of the HZ (d^*_{HZ}), and area of the HZ (A^*_{HZ}) in the first three rows of Figure 4 decrease with increasing upwelling flux (q^*_{gw}). When the low-permeability layer is deep enough (large d^*_l), these metrics match the results for the homogeneous condition ($k_r=1$) and the low-permeability layer has no impact. This threshold is not very deep; it happens for $d^*_l \geq 0.25$ in the case of HEF and $d^*_l \geq 0.60$ in the case of d^*_{HZ} and A^*_{HZ}. In this asymptotic case, the decrease in d^*_{HZ} and A^*_{HZ} as a function of q^*_{gw} is roughly exponential over the range of upwelling and k_r explored, becoming insensitive for $q^*_{gw} \geq 14$. As the low-permeability layer becomes shallow enough (decreasing d^*_l), the net HEF, area, and penetration depth decrease; the area and depth become very sensitive to low values of the permeability ratio, k_r. HEF, q^*_{HZ}, is not very sensitive to this permeability, which is explained by the dominant role of very shallow, fast flow paths in the discharge zone. However, the HEF becomes sensitive to upwelling when $q^*_{gw} \geq 1.4$, decreasing slightly. Similar results were found for a discontinuous low-permeability layer.

3.2.2. RTDs and Its Moments

The bottom three rows of Figure 4 summarize the flux-weighted residence time mean ($\mu^*_{\tau,FW}$), standard deviation ($\sigma^*_{\tau,FW}$), and coefficient of variation ($CV^*_{FW}=\sigma^*_{\tau,FW}/\mu^*_{\tau,FW}$), respectively, for a continuous low-permeability layer. The bottom boundary of the HZ is an interface with ambient groundwater across which there is mixing due to diffusion and dispersion. Groundwater upwelling compresses the HZ and speeds up the dispersive mixing by increasing the specific discharge in the vicinity of this interface. Compression also shortens flow paths, reducing the residence times for flow paths above the interface. In these simulations, the upwelling groundwater is substantial older ($\mu^*_{\tau,GW}=5.51$) than the water in the hyporheic zone. Consequently, the mixing increases the age of the hyporheic flux. The low-permeability layer also compresses the HZ and sequesters circulating water for smaller values of k_r leading to additional aging. This complex interaction of compressed flow paths, mixing, and sequestration leads to increasing mean RT and RT variability as k_r or the depth of the low-permeability layer decrease, or upwelling increases. Both metrics become very sensitive to upwelling when $q^*_{gw} \geq 1.42$, although the coefficient of variation slightly decreases. In the presence of upwelling only, the shallowest ($d^*_l \leq 0.05$) of low-permeability layers appears to have an impact on RT mean and variability, and then only for intermediate $q^*_{gw} \leq 7$. In the absence of upwelling (left most points in all graphs), k_r and depth d^*_l influence RT tailing as shown by the sensitivity of RT variability $\sigma^*_{\tau,FW}$ and CV^*_{FW}; the mean is not affected. Once again, similar results were found for a discontinuous low-permeability layer.

Flux-weighted RTDs (f^*_{FW}) for the HZ evidence multimodality (see Figure 5), which is expected for a nested system of flow paths. For younger ages, $\tau^* \leq 0.01$, the probability density f^* is remarkably similar for both continuous and discontinuous low-permeability layers, a wide range of k_r, and even different strengths of upwelling q^*_{gw} (Figures 5a–5g). It is only when the upwelling flux is sufficiently large, $q^*_{gw} \geq 14$, that any difference appears. This suggests that the shorter, faster HZ flow paths are not significantly influenced by structured heterogeneities or upwelling. In the homogeneous case (upper-right reference case in Figure 5g), as upwelling increases we observe the emergence of a new mode in the late-time behavior of the RTD, which corresponds to the contribution of mixing between HZ water and upwelling groundwater along the HZ boundary. The importance of this mode increases with q^*_{gw}. Under neutral conditions ($q^*_{gw}=0$), the presence of a low-permeability layer (continuous or discontinuous) results in the emergence of a small mode (black line in Figure 5c), which eventually becomes a slightly heavier tail (more memory) as k_r decreases

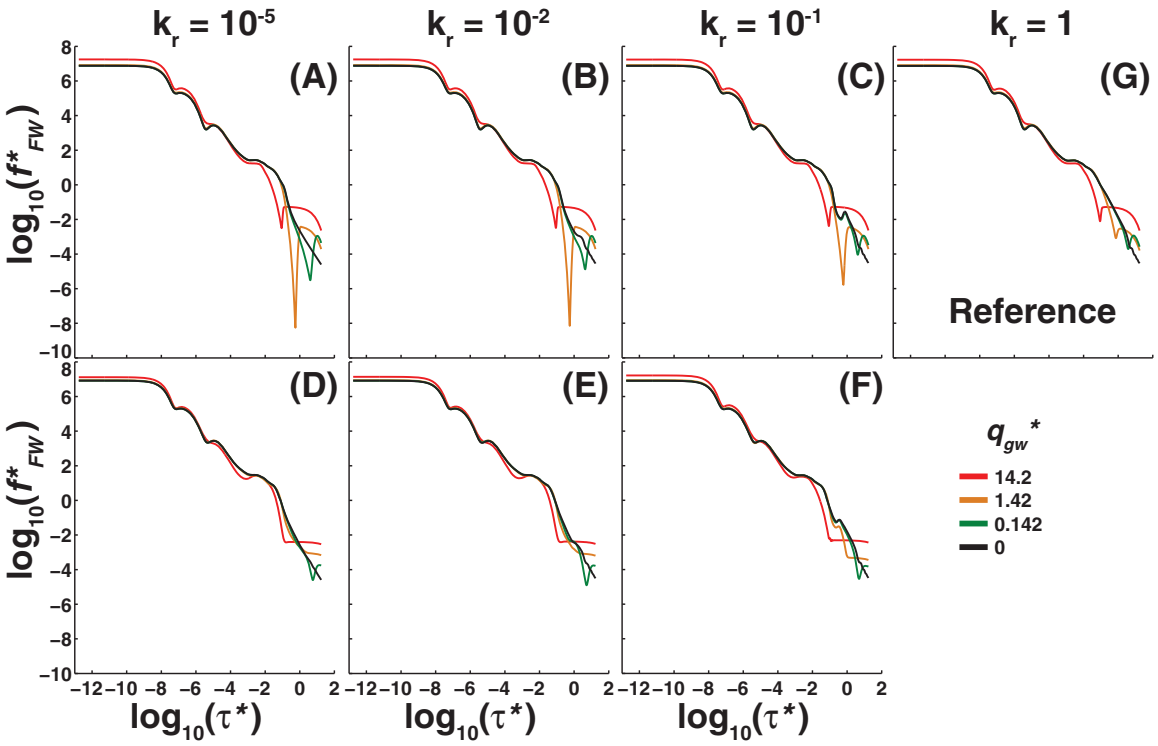

Figure 5. Flux-weighted RTD (f^*_{FW}) for (a–c and g) continuous ($s^* = 0.0$ and $d^*_l = 0.15$) and (d–f) discontinuous ($d^*_l = 0.15$, $s^* = 0.2$, $r^* = 0.6$) scenarios under different ratios of k_r. Colors correspond to different values of groundwater upwelling q^*_{gw}.

(black line in Figure 5a). As the groundwater upwelling increases new modes appear (Figures 5a–5c); their time of appearance decreases with q^*_{gw} but is insensitive to k_r. For the continuous low-permeability layer case the size of the mode is greatest at $q^*_{gw} = 1.4$. Is there something special about this flux condition? It represents a rough balance between horizontal and vertical flow.

3.2.3. When Does Upwelling Dominate?

Upwelling dominates heterogeneity (and to some extent the morphology-driven exchange) when $q^*_{gw} \geq 14$. This is apparent in Figure 5 where the depth of low-permeability layer and the permeability of that layer have essentially no impact on the studied geometric or residence time metrics. HEF is slightly sensitive to depth, but only for a very shallow layer ($d^*_l \leq 0.5$) and it too is insensitive to k_r. In short, upwelling groundwater can dominate if it is strong enough.

3.3. Spatial Patterns of the HZ and Its Residence Times

3.3.1. Geometry of the HZ

The geometry of the HZ changes considerably when low-permeability layers are present. Figure 6 illustrates this by showing the extent of the HZ for a continuous (a and b) and discontinuous (c and d) layer under both neutral (a and c) and gaining (b and d) conditions for several ratios k_r. Decreasing k_r results in smaller HZs and larger fractions of the total HZ being confined to and above the low-permeability zone. From this point of view, even though the HZ becomes smaller its sequestration potential and relative importance increase when the low-permeability layer is contained within the HZ, or when mixing between the HZ and upwelling groundwater takes place in or near the low-permeability layer.

Under neutral conditions ($q^*_{gw} = 0$, Figures 6a and 6c), the presence of discontinuities in the low-permeability layer modestly increases the size of the HZ. This is caused by the circulation cell that appears in the window through the low-permeability layer (see Figure 3c). Under upwelling conditions, the HZ tends to be larger for a discontinuous layer than for a continuous layer, allowing for larger portions of the HZ to

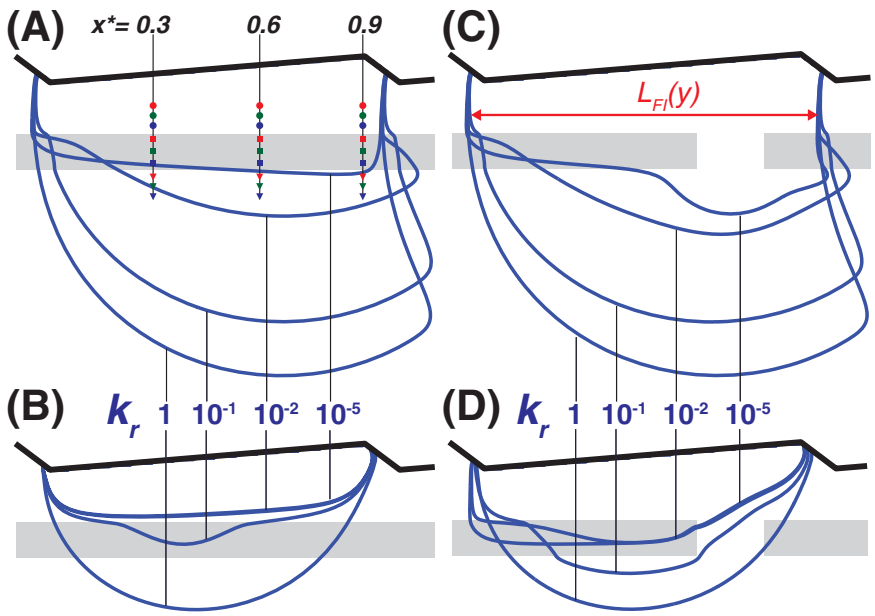

Figure 6. Hyporheic zone extent (blue lines) as a function of k_r (see vertical black lines) for (a and b) continuous ($s^* = 0.0$) and (c and d) funneling scenarios. Figures 6a and 6c and Figures 6b and 6d correspond to $q^*_{gw} = 0$ and $q^*_{gw} = 1.42$, respectively. Points illustrate the individual locations sampled in the sensitivity analysis for the RTD above (circles), within (squares), and below (triangles) the low-permeability layer (gray area). The RTD for the blue circle at $x^* = 0.9$ is shown later in Figure 8. $L_{FI}(y)$ is the length used to estimate the flushing intensities. ($d^*_l = 0.15$, $r^* = 0.6$, and $s^* = 0.2$).

enclose the low-permeability zone. This is explained by the funneling effect of the discontinuity, which focuses upwelling flow and compresses the HZ near the window, while it expands elsewhere.

3.3.2. Spatial Patterns of RT

Spatial variability of mean RT is a key metric to understand the impacts of structural heterogeneity such as our low-permeability layer. Figures 7a-7f show the spatial distribution of the mean RT (μ^*_τ) for the scenarios shown in Figure 3 with $k_r = 10^{-5}$. The color scale is logarithmic, so every contour line corresponds to an order-of-magnitude change in mean RT. Younger water is present along the shallow, short flow paths, which carry most water and solutes through the HZ. Upwelling compresses the HZ and older age contours wane, although younger ones remain essentially unchanged (compare the first and second columns in Figure 7). Consequently, a larger proportion of the remaining HZ is dominated by younger waters (Figures 7a and 7d), a difference sometimes referred to as rejuvenation. A considerable fraction of the HZ overlaps the low-permeability layer, where residence times can be several orders of magnitude older than the rest of the HZ water. This sequestration results in large age gradients along the boundary of the low-conductivity layer.

To evaluate the effect of the permeability contrast between the ambient sediment and the low-permeability layer (decreasing k_r), we use the ratio of the mean RT for $k_r = 10^{-5}$ and a reference case with $k_r = 10^{-1}$. The spatial variability of this metric is shown in Figures 7g–7j. Rejuvenation and aging due to a decrease in k_r are evident in this figure. For example, in the case of a continuous layer under neutral conditions (Figure 7g), a decrease in k_r from $k_r = 10^{-1}$ to $k_r = 10^{-5}$ leads to localized zones of rejuvenation close to the SWI (magenta contours in the figure). This is caused by acceleration due to flow convergence. On the other hand, most of the domain becomes older (white and yellow zones in the figure). A large proportion of the HZ above the low-permeability layer is up to 1 order of magnitude older than the reference case, but the lower part of the HZ in and just above the low-permeability layer has a mean RT that is at least 10 times or larger than the reference case. Similar large increases in RT are observed below the low-permeability layer and HZ.

With this in mind, old and young water mix along the boundary of the low-permeability layer resulting in multimodal and heavy-tailed residence time distributions (see Figure 8). Consider the neutral case with no

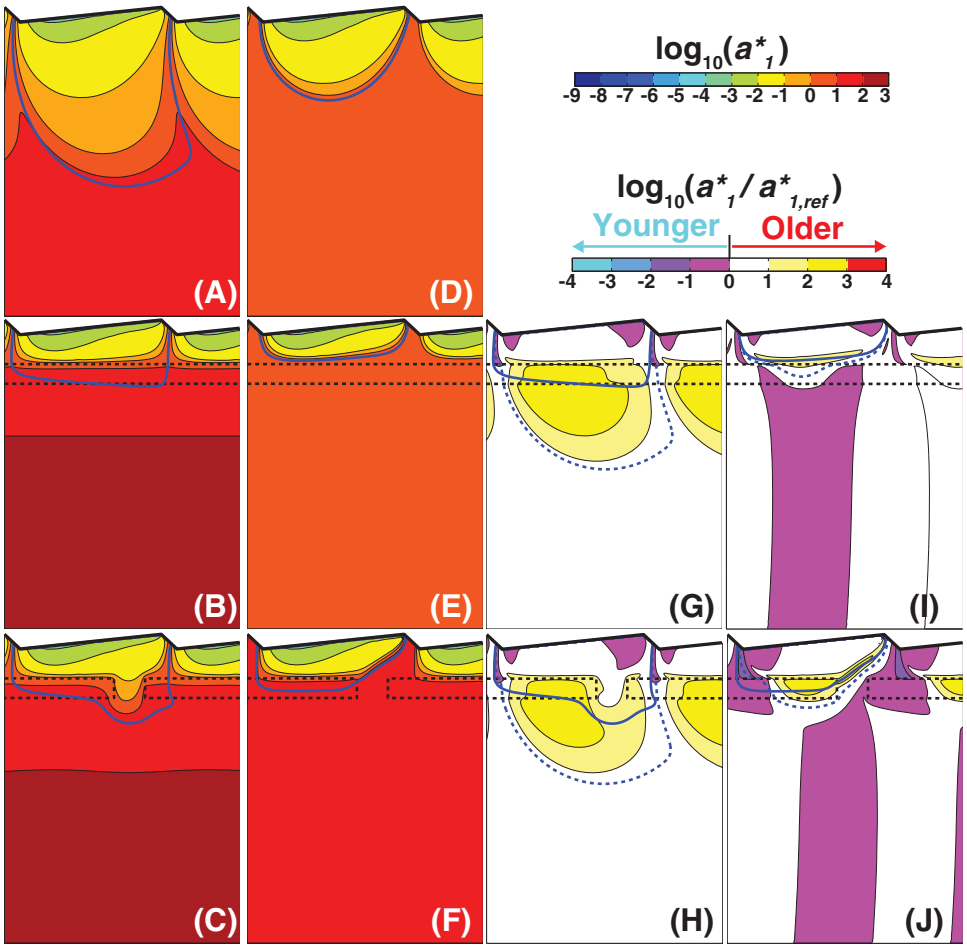

Figure 7. Mean RT under (a–c) neutral and (d–f) upwelling conditions. Solid blue line in Figures 7a–7f corresponds to the extent of the HZ. Ratio of the mean RT for $k_r = 10^{-5}$ and $k_r = 10^{-1}$ under (g and h) neutral and (I and j) upwelling conditions. Solid and dashed blue lines in Figures 7g–7j correspond to the extent of the HZ for $k_r = 10^{-5}$ and $k_r = 10^{-1}$, respectively. From top to bottom, rows correspond to homogeneous ($k_r = 1$), continuous ($k_r = 10^{-5}$), and funneling ($k_r = 10^{-5}$, $s^* = 0.2$, and $r^* = 0.6$) cases. Upwelling scenarios use $q^*_{gw} = 1.42$.

upwelling (Figure 8a). When the permeability is homogeneous (black circles corresponding to $k_r = 1$), unimodality and light tailing is observed; (note: the wiggles for $\tau^* \geq 5$ represent numerical oscillations, not new modes). As k_r decreases, a second mode appears representing the accumulation of RT within the low-permeability layer appears (blue circles corresponding to $k_r = 10^{-1}$). The low-permeability layer constraints HZ flow resulting in an earlier peak for the first mode. Eventually, for smaller k_r values, the second mode is damped and delayed (green circles corresponding to $k_r = 10^{-2}$) and heavy tailing emerges ($k_r = 10^{-2}$ to 10^{-5}), which can be interpreted as long-term memory or sequestration (magenta circles corresponding to $k_r = 10^{-5}$). When the low-permeability layer is present the first mode appears at essentially the same age, no matter what the permeability, and when $k_r \geq 10^{-2}$ the peak height remains the same, as if that permeability is a threshold for controlling residence time in the hyporheic zone above the layer.

Figure 8b illustrates the case where the HZ is pushed above the low-permeability layer by upwelling (see Figures 3f and 7f). In this situation, multimodality occurs for all cases, even the homogeneous case. It is explained by the local circulation of the HZ (first mode) and mixing with older upwelling groundwater along the HZ boundary (second mode). As in the neutral case, when the low-permeability zone is present the first mode appears at essentially the same time, and when $k_r \geq 10^{-2}$ the peak height remains the same. Demonstrating the consistency of mixing the second mode timing and peak is the same for all values of $k_r > 0$.

The location studied for Figure 8 is depicted in Figure 6. It was selected to be near the HZ boundary with an opportunity to mix different water sources (see the flow and HZ patterns in Figures 3, 6, and 7). We also

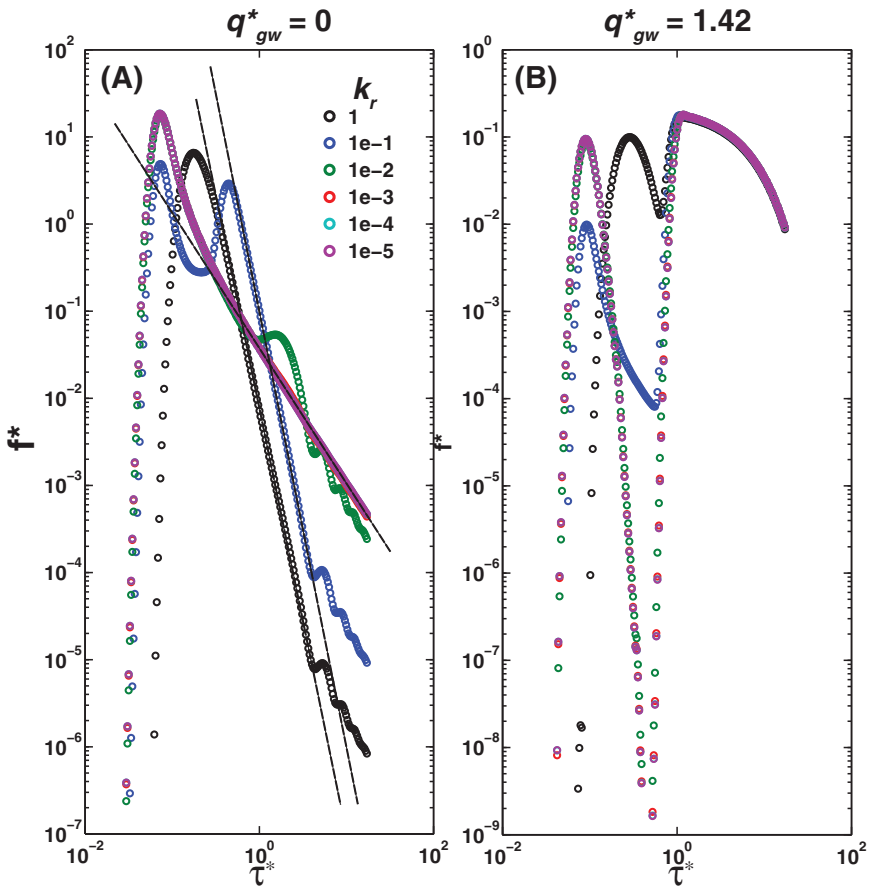

Figure 8. RTDs (f^*) as a function of dimensionless RT (τ^*) obtained near the upper boundary of the continuous low-permeability layer located at $d_l^* = 0.15$ (blue circle at $x^* = 0.9$ in Figure 6) under (a) neutral and (b) upwelling $q^*_{gw} = 1.42$ conditions. Colors correspond to different values of the ratio k_r.

studied the other point locations in Figure 6 and did so for a variety of depths d_l^*. Consistent results were obtained for points selected to be near the HZ boundary.

3.3.3. Flushing Intensity

Water flushing intensity is a measure of the average local capacity to mobilize water and solutes by advection and is defined as [after *Zlotnik et al.*, 2010]:

$$FI(y) = \frac{1}{L_{FI}(y)} \int_0^{L_{FI}(y)} |\mathbf{q}(x,y)| \mathrm{d}x \tag{10}$$

where $L_{FI}(y)$ is the width of the HZ at a depth y (see Figure 6c). Notice that we modified the original definition by *Zlotnik et al.* [2010] in order to focus on the flushing capacity of the HZ and not of the whole system. With a similar spirit, we also introduce an RT-weighted flushing intensity, which accounts for the fact that having high water flushing capacity does not necessarily imply that the water being flushed is old. The RT-weighted flushing intensity is defined as

$$FI_{RT}(y) = \frac{1}{L_{FI}(y) FI(y)} \int_0^{L_{FI}(y)} \mu_\tau(x,y) |\mathbf{q}(x,y)| \mathrm{d}x \tag{11}$$

The flushing intensities are expressed in dimensionless terms as $FI^*(y) = FI(y)/q_c$ and $FI^*_{RT}(y) = FI_{RT}(y)/t_c$.

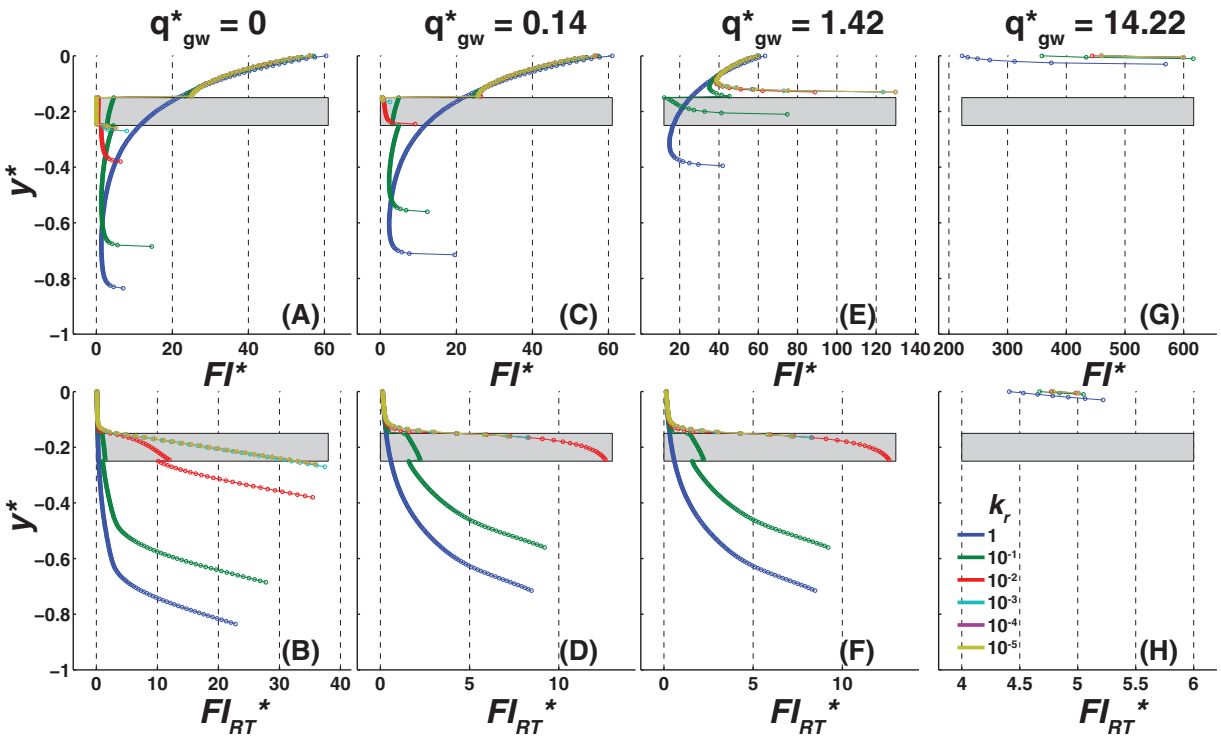

Figure 9. Vertical variation (y^*) of the (a, c, e, and g) flushing intensity of water (Fl^*) and (b, d, f, and h) mean RT (Fl^*_{RT}) for continuous ($s^* = 0.0$) scenarios under different groundwater upwelling fluxes q^*_{gw} (columns). Colors correspond to different values of the ratio k_r, gray area corresponds to the location of the low-permeability layer, and $d^*_l = 0.15$ in all cases.

Flushing intensity is used to evaluate the importance of the RT accumulation at the upper boundary of the low-permeability layer. Figure 9 presents water flushing intensities $Fl^*(y)$ (plot a, c, e, and g) and RT-weighted flushing intensities $Fl^*_{RT}(y)$ (plot b, d, f, and h) for a variety of groundwater upwelling scenarios (columns) and ratios k_r. Patterns for the discontinuous layers are similar (not shown). For a prescribed upwelling rate, the flushing intensities above the low-permeability layer remain similar across all heterogeneous scenarios as well as the homogeneous ($k_r = 1$) case. The convergence of flow paths caused by heterogeneity increase water flushing intensity $Fl^*(y)$ near the boundary with the low-permeability layer and RT-flushing intensity $Fl^*_{RT}(y)$ within the low-permeability layer; both effects are amplified by increases in groundwater upwelling (see Figures 9a, 9c, and 9e).

3.4. Hydrodynamics and Possible Biogeochemical Implications

Biogeochemistry is not the focus of this manuscript; however, understanding the role of low-permeability layers on the HZ's biogeochemical cycling, buffering potential, and aquatic ecology is an important motivation. In this section, we briefly illustrate the possible implications that hydrodynamic changes (i.e., changes in fluxes and RTs) have on the biogeochemistry of these complex systems when residence time is used as a master variable in biogeochemical evolution [*Zarnetske et al.*, 2011a]. As explained in the following paragraphs, statements based in this simple conceptualization can be biased and are only intended to guide future detailed experimental observations and multispecies biogeochemical modeling [see, for example, *Bardini et al.*, 2013].

Comparisons between residence times and characteristic times for biogeochemical reactions have been used to explain biogeochemical evolution within hyporheic zones, specifically to classify them as net sources or sinks of solutes, nutrients, and contaminants [see, for example, *Gomez et al.*, 2012; *Zarnetske et al.*, 2012; *Marzadri et al.*, 2012; *Harvey et al.*, 2013]. From a basic perspective, short hyporheic residence times are likely to be associated with aerobic conditions, and therefore aerobic respiration, nitrification, and other oxidizing reactions (e.g., manganese, iron, and sulfide oxidation) [*Harvey and Fuller*, 1998; *Fuller and Harvey*, 2000] within the hyporheic zone. With increasing RT and continuing oxygen consumption anaerobic conditions

prevail when dissolved oxygen is depleted, leading to reducing reactions such as denitrification, metal reduction, sulfide reduction, and methanogenesis. As these processes are microbially mediated, flow and biogeochemical patterns feedback with the spatial distribution of bacterial communities [*Chapelle*, 2000]. This conceptualization is appropriate for simple advection-dominated hyporheic zones with uniform and well-defined solute sources, chemically homogeneous sediments, and without large-scale groundwater fluxes. That is, in cases where a stream tube model, like the one used by *Marzadri et al*. [2012], adequately represents the hydrodynamics and biogeochemical evolution of the HZ. In general, this is not the case when groundwater upwelling and low-permeability layers are present, given the importance of mixing between waters with different biogeochemical signature and the presence of chemical and biological heterogeneity within the sediment.

As shown in the previous section, the presence of low-permeability layers leads to important changes in the intensity of hyporheic exchange and the shape of the HZ both under neutral and upwelling conditions. Given the dominating influence of shallow, unaffected flow paths to the total HEF, the net effect on integrated RTDs at the outlet of the HZ is negligible and this metric does not give sufficient information to evaluate the net effect of large-scale heterogeneities. As biogeochemical reactivity in streambeds has been shown to be spatially variable, with hot spots of biogeochemical turnover coinciding with structural heterogeneities [e.g., *Krause et al*., 2013], spatial variability of residence times may provide a better metric to evaluate the possible biogeochemical zonation within the hyporheic zone.

Systems with nested scales of interaction, like the one studied in this work, are characterized by hydrodynamic sequestration and aging due to deceleration around stagnation zones [e.g., *Jiang et al*., 2011, 2012, 2014]. The presence of low-permeability zones induces additional sequestration. Their significance depends on the proportion of the HZ that is affected by this heterogeneity. Our simulations show that decreasing permeability of the low-permeability layers results in smaller HZs and larger fractions of the total HZ being confined to the low-permeability zone. From this point of view, even though the HZ is smaller, the sequestration potential and its relative importance dramatically increases. Permeability contrasts of 2–5 orders of magnitude are commonly found in natural environments [e.g., *Kennedy et al*., 2009a; *Naranjo et al*., 2013; *Krause et al*., 2013], leading to scenarios like the ones shown in Figure 7 for $k_r < 10^{-2}$. The heterogeneities not only influence sequestration but also the spatial location and number of stagnation zones leading to a variety of aging patterns.

For some depositional environments, the low-permeability layers can have considerable amounts of organic matter (e.g., peat deposits) [*Krause et al*., 2013]. In such cases, these streambed features represent an autochthonous source of potentially bioavailable organic carbon essential for aerobic as well as anaerobic microbial metabolic activity. In consequence, the heterogeneous spatial patterns of these organic-rich structures can create microenvironments where facultative (an)aerobe respirers and obligate anaerobes are able to perform at high efficiency and metabolize under anaerobic conditions after consumption of dissolved oxygen [*Chapelle*, 2000]. In this situation, the mixing of end-member waters at the interface of the low-permeability layer becomes critical, since addition of bioavailable dissolved organic carbon at the interface of the low-permeability layer can mix with oxygenated hyporheic water as well as upwelling (in lowland catchments often nutrient enriched) groundwater, resulting in enhanced denitrification [*Zarnetske et al*., 2011b] aided by fast mobilization due to high flushing intensities.

4. Conclusions

Low-permeability layers have a minimal impact on the flux-weighted RTDs for water discharging to the stream. This is explained by the low contribution to the total HZ discharge of the flow paths affected by these layers. Enhanced dispersive mixing, between the HZ and the upwelling groundwater, increases with upwelling fluxes and results in a new characteristic mode of the HZ RTD. In general, the integrated RTD is not the ideal metric to evaluate the role of low-permeability layers in bed form-driven hyporheic exchange.

Our simulations show that spatial patterns of RTDs and its moments are more useful than flux-weighted RTDs to evaluate the implications of structural heterogeneity for biogeochemical transformations. Application of this principle indicates that the interface of the low-permeability layers is expected to be a hot spot

for biogeochemical transformations, given its capacity to mix older sequestered waters, younger hyporheic waters, and even older upwelling groundwater. Additionally, these locations present significant flushing intensities, indicating a high potential to mobilize the products of redox chemical and microbial processes at the interface.

Future research focusing on the multispecies modeling of the biogeochemical evolution along different flow paths within the hyporheic zone will be needed to represent the overall efficiency and spatial patterns of biogeochemical turnover for the scenarios explored in this manuscript in order to quantify hot spot behavior of these streambed heterogeneous structures.

Appendix A: Residence Time Model

Assuming steady flow and no sources or sinks, the spatial evolution of RTD f is described by:

$$\theta \frac{\partial f}{\partial \tau} = \nabla \cdot (\mathbf{D}\nabla f - \mathbf{q}f) \tag{A1a}$$

$$f(\mathbf{x}, \tau) = \delta(\tau) \text{ for } \partial\Omega_{in} \tag{A1b}$$

$$\mathbf{n} \cdot (\mathbf{D}\nabla f) = 0 \text{ for } \partial\Omega_{out} \tag{A1c}$$

$$f(x = -L, y, \tau) = f(x = 2L, y, \tau) \text{ for } \partial\Omega_u \text{ and } \partial\Omega_d \tag{A1d}$$

$$(1 - \eta_{gw})[\mathbf{n} \cdot (\mathbf{q}f - \mathbf{D}\nabla f)] + \eta_{gw} q_{gw}[f - f_{gw}] = 0 \text{ for } \partial\Omega_b \tag{A1e}$$

where f_{gw} $[T^{-1}]$ is the RTD of the upwelling groundwater and the hydrodynamic transport operator $\nabla \cdot (\mathbf{D}\nabla f - \mathbf{q}f)$ considers Darcy's scale advection and Fickian dispersion. See *Ginn* [1999], *Gomez et al.* [2012], and *Gomez and Wilson* [2013] for a detailed description of the theory and implementation of RTD models. Incorporating effective porosity implicitly in (12), the dispersion-diffusion tensor $\mathbf{D} = \{D_{ij}\}$ is defined as [*Bear*, 1972]:

$$D_{ij} = \alpha_T |\mathbf{q}| \delta_{ij} + (\alpha_L - \alpha_T) \frac{q_i q_j}{|\mathbf{q}|} + \epsilon D_m \tag{A2}$$

with α_T and α_L the transverse and longitudinal dispersivities, respectively, D_m the molecular diffusion coefficient, ϵ the tortuosity factor, δ_{ij} the Kronecker delta function, and η_{up} a binary function that distinguishes between neutral and upwelling groundwater flow conditions

$$\eta_{gw} = \begin{cases} 0 & \text{for neutral groundwater flow } (q_{gw} = 0) \\ 1 & \text{for upwelling groundwater flow } (q_{gw} > 0) \end{cases} \tag{A3}$$

Note that the model for the evolution of F can be obtained by integrating equation (A1) [see *Gomez and Wilson*, 2013] and the porosity is incorporated in the definition of $\mathbf{D}$ as written here.

The model for the moments, a_n, $n = 1, 2, \ldots$, and $a_0(\mathbf{x}, t) = 1$ is [*Varni and Carrera*, 1998; *Gomez and Wilson*, 2013]:

$$\nabla \cdot (\mathbf{D}\nabla a_n - \mathbf{q}a_n) = -n\theta a_{n-1} \tag{A4a}$$

$$a_n(\mathbf{x}) = 0 \text{ for } \partial\Omega_{in} \tag{A4b}$$

$$\mathbf{n} \cdot (\mathbf{D}\nabla a_n) = 0 \text{ for } \partial\Omega_{out} \tag{A4c}$$

$$a_n(x=-L, y) = a_n(x=2L, y) \text{ for } \partial\Omega_u \text{ and } \partial\Omega_d \tag{A4d}$$

$$(1-\eta_{gw})[\mathbf{n} \cdot (\mathbf{q}a_n - \mathbf{D}\nabla a_n)] + \eta_{gw} q_{gw}[a_n - a_{n,gw}] = 0 \text{ for } \partial\Omega_b \tag{A4e}$$

Acknowledgments
This research was funded by the National Science Foundation through the New Mexico EPSCoR Track I-II (award EAR 0814449) and the project Dynamic Groundwater Age Distributions: Exploring Watershed Scale Subsurface Systems (award EAR 1015100) awarded to New Mexico Tech. Additional funding was provided by an American Geophysical Union Horton Research grant and a New Mexico Water Resources Research Institute Student grant awarded to Jesus D. Gomez-Velez. The authors thank C. N. Dahm, W. D. Stone, M. Person, and F. M. Phillips at New Mexico Tech and J. W. Harvey at USGS for their valuable suggestions regarding this article.

References

Acuña, V., and K. Tockner (2009), Surface-subsurface water exchange rates along alluvial river reaches control the thermal patterns in an alpine river network, *Freshwater Biol.*, *54*, 306–320.

Angermann, L., S. Krause, and J. Lewandowski (2012), Application of heat pulse injections for investigating shallow hyporheic flow in a lowland river, *Water Resour. Res.*, *48*, W00P02, doi:10.1029/2012WR012564.

Arrigoni, A. S., G. C. Poole, L. A. K. Mertes, S. J. O'Daniel, W. W. Woessner, and S. A. Thomas (2008), Buffered, lagged, or cooled? Disentangling hyporheic influences on temperature cycles in stream channels, *Water Resour. Res.*, *44*, W09418, doi:10.1029/2007WR006480.

Bardini, L., F. Boano, M. B. Cardenas, R. Revelli, and L. Ridolfi (2012), Nutrient cycling in bedform induced hyporheic zones, *Geochim. Cosmochim. Acta*, *84*, 47–61, doi:10.1016/j.gca.2012.01.025.

Bardini, L., F. Boano, M. B. Cardenas, A. H. Sawyer, R. Revelli, and L. Ridolfi (2013), Small-scale permeability heterogeneity has negligible effects on nutrient cycling in streambeds, *Geophys. Res. Lett.*, *40*, 1118–1122, doi:10.1002/grl.50224.

Battin, T., L. A. Kaplan, S. Findlay, C. S. Hopkinson, E. Marti, A. I. Packman, J. D. Newbold, and F. Sabater (2008), Biophysical controls on organic carbon fluxes in fluvial networks, *Nat. Geosci.*, *1*, 95–100, doi:10.1038/ngeo101.

Bear, J. (1972), *Dynamics of Fluids in Porous Media*, Elsevier, N. Y.

Bhaskar, A. S., J. W. Harvey, and E. J. Henry (2012), Resolving hyporheic and groundwater components of streambed water flux using heat as a tracer, *Water Resour. Res.*, *48*, W08524, doi:10.1029/2011WR011784.

Boano, F., R. Revelli, and L. Ridolfi (2007), Bedform-induced hyporheic exchange with unsteady flows, *Adv. Water Resour.*, *30*, 148–156.

Boano, F., R. Revelli, and L. Ridolfi (2008), Reduction of the hyporheic zone volume due to the stream-aquifer interaction, *Geophys. Res. Lett.*, *35*, L09401, doi:10.1029/2008GL033554.

Boano, F., R. Revelli, and L. Ridolfi (2009), Quantifying the impact of groundwater discharge on the surface-subsurface exchange, *Hydrol. Processes*, *23*(15), 2108–2116, doi:10.1002/hyp.7278.

Boano, F., R. Revelli, and L. Ridolfi (2011), Water and solute exchange through flat streambeds induced by large turbulent eddies, *J. Hydrol.*, *402*, 290–296.

Boulton, A. J., and P. J. Hancock (2006), Rivers as groundwater-dependent ecosystems: A review of degrees of dependency, riverine processes and management implications, *Aust. J. Bot.*, *54*(2), 133–144.

Brayshaw, A. C., G. W. Davies, and P. W. M. Corbett (1996), Depositional controls on primary permeability and porosity at the bedform scale in fluvial reservoir sandstones, in *Advances in Fluvial Dynamics and Stratigraphy*, edited by P. Carling and M. Dawson, pp. 373–394, John Wiley, Chichester, U. K.

Briggs, M., L. Lautz, J. McKenzie, R. Gordon, and D. Hare (2012), Using high resolution distributed temperature sensing to quantify spatial and temporal variability in vertical hyporheic flux, *Water Resour. Res.*, *48*, W02527, doi:10.1029/2011WR011227.

Brunke, M., and T. Gonser (1997), The ecological significance of exchange processes between rivers and groundwater, *Freshwater Biol.*, *37*(1), 1–33.

Buffington, J. M., and D. Tonina (2009), Hyporheic exchange in mountain rivers ii: Effects of channel morphology on mechanics, scales, and rates of exchange, *Geogr. Compass*, *3*(3), 1063–1086, doi:10.1111/j.1749-8198.2009.00225.x.

Burkholder, B. K., G. Grant, R. Haggerty, T. Khangaonkar, and P. Wampler (2008), Influence of hyporheic flow and geomorphology on temperature of a large, gravel-bed river, Clackamas River, Oregon, USA, *Hydrol. Processes*, *22*(7), 941–953.

Cardenas, M., J. L. Wilson, and V. Zlotnik (2004), Impact of heterogeneity, bed forms, and stream curvature on subchannel hyporheic exchange, *Water Resour. Res.*, *40*, W08307, doi:10.1029/2004WR003008.

Cardenas, M. B. (2008), Surface water-groundwater interface geomorphology leads to scaling of residence times, *Geophys. Res. Lett.*, *35*, L08402, doi:10.1029/2008GL033753.

Cardenas, M. B., and J. Wilson (2006), The influence of ambient groundwater discharge on exchange zones induced by current–bedform interactions, *J. Hydrol.*, *331*, 103–109, doi:10.1016/j.jhydrol.2006.05.012.

Cardenas, M. B., and J. L. Wilson (2007a), Effects of current-bed form induced fluid flow on the thermal regime of sediments, *Water Resour. Res.*, *43*, W08431, doi:10.1029/2006WR005343.

Cardenas, M. B., and J. L. Wilson (2007b), Hydrodynamics of coupled flow above and below a sediment-water interface with triangular bedforms, *Adv. Water Resour.*, *30*, 301–313, doi:10.1016/j.advwatres.2006.06.009.

Cardenas, M. B., and J. L. Wilson (2007c), Exchange across a sediment–water interface with ambient groundwater discharge, *J. Hydrol.*, *346*, 69–80, doi:10.1016/j.jhydrol.2007.08.019.

Cardenas, M. B., and J. L. Wilson (2007d), Dunes, turbulent eddies, and interfacial exchange with permeable sediments, *Water Resour. Res.*, *43*, W08412, doi:10.1029/2006WR005787.

Cardenas, M. B., J. L. Wilson, and R. Haggerty (2008), Residence time of bedform-driven hyporheic exchange, *Adv. Water Resour.*, *31*, 1382–1386, doi:10.1016/j.advwatres.2008.07.006.

Chapelle, F. H. (2000), *Ground-Water Microbiology and Geochemistry*, 2nd ed., 496 pp., John Wiley, N. Y.

Conant, B. (2004), Delineating and quatifying ground water discharge zones using streambed temperatures, *Ground Water*, *42*(2), 243–257.

Corcho-Alvarado, J. A., R. Purtschert, F. Barbecot, C. Chabault, J. Rueedi, V. Schneider, W. Aeschbach-Hertig, R. Kipfer, and H. H. Loosli (2007), Constraining the age distribution of highly mixed groundwater using 39Ar: A multiple environmental tracer (3H/3He, 85Kr, 39Ar, and 14C) study in the semiconfined Fontainebleau Sands Aquifer (France), *Water Resour. Res.*, *43*, W03427, doi:10.1029/2006WR005096.

Crispell, J. K., and T. A. Endreny (2009), Hyporheic exchange flow around constructed in-channel structures and implications for restoration design, *Hydrol. Processes*, *23*, 1158–1168, doi:10.1002/hyp.7230.

Domenico, P., and F. W. Schwartz (1990), *Physical and Chemical Hydrogeology*, John Wiley, N. Y.

Dullien, F. A. L. (1991), *Fluid Transport and Pore Structure*, 2nd ed., 574 pp., Academic Press, San Diego, Calif.
Elliott, A. H., and N. H. Brooks (1997), Transfer of nonsorbing solutes to a streambed with bed forms: Laboratory experiments, *Water Resour. Res.*, *35*(1), 137–151.
Endreny, T., L. Lautz, and D. I. Siegel (2011), Hyporheic flow path response to hydraulic jumps at river steps: Flume and hydrodynamic models, *Water Resour. Res.*, *47*, W02517, doi:10.1029/2009WR008631.
Endreny, T. A., and L. K. Lautz (2012), Comment on "Reducing monitoring gaps at the aquifer–river interface by modelling groundwater–surfacewater exchange flow patterns" by M. Munz, S. Krause, C. Tecklenburg, and A. Binley, *Hydrol. Processes*, *26*, 1586–1588, doi: 10.1002/hyp.8410.
Fanelli, R., and L. Lautz (2008), Patterns of water, heat and solute flux through streambeds around small dams, *Ground Water*, *46*(5), 671–687.
Fox, A., F. Boano, and S. Arnon (2014), Impact of losing and gaining streamflow conditions on hyporheic exchange fluxes induced by dune-shaped bed forms, *Water Resour. Res.*, *50*, 1895–1907, doi:10.1002/2013WR014668.
Freeze, R., and J. Cherry (1979), *Groundwater*, Prentice Hall, Upper Saddle River, N. J.
Frisbee, M. D., F. M. Phillips, A. R. Campbell, F. Liu, and S. A. Sanchez (2011), Streamflow generation in a large, alpine watershed in the southern Rocky Mountains of Colorado: Is streamflow generation simply the aggregation of hillslope runoff responses?, *Water Resour. Res.*, *47*, W06512, doi:10.1029/2010WR009391.
Frisbee, M. D., J. L. Wilson, J. D. Gomez-Velez, F. M. Phillips, and A. R. Campbell (2013), Are we missing the tail (and the tale) of residence-time distributions in watersheds?, *Geophys. Res. Lett.*, *40*, 4633–4637, doi:10.1002/grl.50895.
Fuller, C. C., and J. W. Harvey (2000), Reactive uptake of trace metals in the hyporheic zone of a mining-contaminated stream, Pinal Creek, Arizona, *Environ. Sci. Technol.*, *34*(7), 1150–1155, doi:10.1021/es990714d.
Gelhar, L., C. Welty, and K. Rehfeldt (1992), A critical review of data on field-scale dispersion in aquifers, *Water Resour. Res.*, *28*(7), 1955–1974.
Genereux, D., S. Leahy, H. Mitasova, C. Kennedy, and D. Corbett (2008), Spatial and temporal variability of streambed hydraulic conductivity in West Bear Creek, North Carolina, USA, *J. Hydrol.*, *358*, 332–353, doi:10.1016/j.jhydrol.2008.06.017.
Ginn, T. R. (1999), On the distribution of multicomponent mixtures over generalized exposure time in subsurface flow and reactive transport: Foundations, and formulations for groundwater age, chemical heterogeneity, and biodegradation, *Water Resour. Res.*, *35*(5), 1395–1407.
Gomez, J. D., and J. L. Wilson (2013), Age distributions and dynamically changing hydrologic systems: Exploring topography-driven regional groundwater flow, *Water Resour. Res.*, *49*, 1503–1522, doi:10.1002/wrcr.20127.
Gomez, J. D., J. L. Wilson, and M. B. Cardenas (2012), Residence time distributions in sinuosity-driven hyporheic zones and their biogeochemical effects, *Water Resour. Res.*, *48*, W09533, doi:10.1029/2012WR012180.
Gooseff, M. N. (2010), Defining hyporheic zones—Advancing our conceptual and operational definitions of where stream water and groundwater meet, *Geogr. Compass*, *4*(8), 945–955, doi:10.1111/j.1749-8198.2010.00364.x.
Gu, C., G. M. Hornberger, A. L. Mills, J. S. Herman, and S. A. Flewelling (2007), Nitrate reduction in streambed sediments: Effects of flow and biogeochemical kinetics, *Water Resour. Res.*, *43*, W12413, doi:10.1029/2007WR006027.
Gu, C., G. M. Hornberger, J. S. Herman, and A. L. Mills (2008), Effect of freshets on the flux of groundwater nitrate through streambed sediments, *Water Resour. Res.*, *44*, W05415, doi:10.1029/2007WR006488.
Harleman, D., P. Melhorn, and R. Rumer (1963), Dispersion-permeability correlation in porous media, *J. Hydraul. Div.*, *89*(2), 67–85.
Harvey, J. W., and C. C. Fuller (1998), Effect of enhanced manganese oxidation in the hyporheic zone on basin-scale geochemical mass balance, *Water Resour. Res.*, *34*(4), 623–636.
Harvey, J. W., J. K. Böhlke, M. A. Voytek, D. Scott, and C. R. Tobias (2013), Hyporheic zone denitrification: Controls on effective reaction depth and contribution to whole-stream mass balance, *Water Resour. Res.*, *49*, 6298–6316, doi:10.1002/wrcr.20492.
Hassan, M. A., D. Tonina, R. D. Beckie, and M. Kinnear (2014), The effects of discharge and slope on hyporheic flow in step-pool morphologies, *Hydrol. Processes*, doi: 10.1002/hyp.10155.
Hayashi, M., and D. Rosenberry (2001), Effects of groundwater exchange on the hydrology and ecology of surface waters, *J. Groundwater Hydrol.*, *43*(4), 327–341.
Huyakorn, P., and G. Pinder (1983), *Computational Methods in Subsurface Flow*, 3rd ed., Academic, Orlando, Fla.
Janssen, F., M. B. Cardenas, A. H. Sawyer, T. Dammrich, J. Krietsch, and D. de Beer (2012), A comparative experimental and multiphysics computational fluid dynamics study of coupled surface-subsurface flow in bed forms, *Water Resour. Res.*, *48*, W08514, doi:10.1029/2012WR011982.
Jiang, X. W., X. S. Wang, L. Wan, and S. Ge (2011), An analytical study on stagnant points in nested flow systems in basins with depth-decaying hydraulic conductivity, *Water Resour. Res.*, *47*, W01512, doi:10.1029/2010WR009346.
Jiang, X.-W., L. Wan, S. Ge, G.-L. Cao, G.-C. Hou, F.-S. Hu, X.-S. Wang, H. Li, and S.-H. Liang (2012), A quantitative study on accumulation of age mass around stagnation points in nested flow systems, *Water Resour. Res.*, *48*, W12502, doi:10.1029/2012WR012509.
Jiang, X.-W., L. Wan, J.-Z. Wang, B.-X. Yin, W.-X. Fu, and C.-H. Lin (2014), Field identification of groundwater flow systems and hydraulic traps in drainage basins using a geophysical method, *Geophys. Res. Lett.*, *41*, 2812–2819, doi:10.1002/2014GL059579.
Kasahara, T., and A. R. Hill (2007), Lateral hyporheic zone chemistry in an artificially constructed gravel bar and a ReMeandered stream channel, southern ontario, canada1, *J. Am. Water Resour. Assoc.*, *43*(5), 1257–1269.
Kasahara, T., and S. M. Wondzell (2003), Geomorphic controls on hyporheic exchange flow in mountain streams, *Water Resour. Res.*, *39*(1), 1005, doi:10.1029/2002WR001386.
Kaser, D. H., A. Binley, A. L. Heathwaite, and S. Krause (2009), Spatio-temporal variations of hyporheic flow in a riffle-step-pool sequence, *Hydrol. Processes*, *23*, 2138–2149, doi:10.1002/hyp.7317.
Kennedy, C. D., D. P. Genereux, D. R. Corbett, and H. Mitasova (2009a), Spatial and temporal dynamics of coupled groundwater and nitrogen fluxes through a streambed in an agricultural watershed, *Water Resour. Res.*, *45*, W09401, doi:10.1029/2008WR007397.
Kennedy, C. D., D. P. Genereux, D. R. Corbett, and H. Mitasova (2009b), Relationships among groundwater age, denitrification, and the coupled groundwater and nitrogen fluxes through a streambed, *Water Resour. Res.*, *45*, W09402, doi:10.1029/2008WR007400.
Koltermann, C. E., and S. M. Gorelick (1995), Fractional packing model for hydraulic conductivity derived from sediment mixtures, *Water Resour. Res.*, *31*(12), 3283–3297, doi:10.1029/95WR02020.
Krause, S., L. Heathwaite, A. Binley, and P. Keenan (2009), Nitrate concentration changes at the groundwater-surface water interface of a small Cumbrian river, *Hydrol. Processes*, *23*, 2195–2211, doi:10.1002/hyp.7213.
Krause, S., D. M. Hannah, J. H. Fleckenstein, C. M. Heppell, D. Kaeser, R. Pickup, G. Pinay, A. L. Robertson, and P. J. Wood (2011a), Inter-disciplinary perspectives on processes in the hyporheic zone, *Ecohydrology*, *4*, 481–499, doi:10.1002/eco.176.

Krause, S., D. M. Hannah, and T. Blume (2011b), Interstitial pore-water temperature dynamics across a pool-riffle-pool sequence, *Ecohydrology*, *4*, 549–563, doi:10.1002/eco.199.

Krause, S., T. Blume, and N. J. Cassidy (2012a), Investigating patterns and controls of groundwater up-welling in a lowland river by combining fibre-optic distributed temperature sensing with observations of vertical hydraulic gradients, *Hydrol. Earth Syst. Sci.*, *16*, 1775–1792, doi:10.5194/hess-16–1775-2012.

Krause, S., M. Munz, C. Tecklenburg, and A. Binley (2012b), The effect of groundwater forcing on hyporheic exchange: Reply to comment on "Munz M., Krause S., Tecklenburg C., Binley A. Reducing monitoring gaps at the aquifer-river interface by modelling groundwater-surfacewater exchange flow patterns", *Hydrol. Processes*, *26*, 1589–1592, doi:10.1002/hyp.9271.

Krause, S., C. Tecklenburg, M. Munz, and E. Naden (2013), Streambed nitrogen cycling beyond the hyporheic zone: Flow controls on horizontal patterns and depth distribution of nitrate and dissolved oxygen in the upwelling groundwater of a lowland river, *J. Geophys. Res. Biogeosci.*, *118*, 54–67, doi:10.1029/2012JG002122.

Leek, R., J. Q. Wu, L. Wang, T. P. Hanrahan, M. E. Barber, and H. Qiu (2009), Heterogeneous characteristics of streambed saturated hydraulic conductivity of the Touchet River, south eastern Washington, USA, *Hydrol. Processes*, *23*, 1236–1246, doi:10.1002/hyp.7258.

Marion, A., A. I. Packman, M. Zaramella, and A. Bottacin-Busolin (2008), Hyporheic flows in stratified beds, *Water Resour. Res.*, *44*, W09433, doi:10.1029/2007WR006079.

Marzadri, A., D. Tonina, and A. Bellin (2012), Morphodynamic controls on redox conditions and on nitrogen dynamics within the hyporheic zone: Application to gravel bed rivers with alternate-bar morphology, *J. Geophys. Res.*, *117*, G00N10, doi:10.1029/2012JG001966.

McGuire, K. J., and J. J. McDonnell (2006), A review and evaluation of catchment transit time modeling, *J. Hydrol.*, *330*(3-4), 543–563, doi:10.1016/j.jhydrol.2006.04.020.

Munz, M., S. Krause, C. Tecklenburg, and A. Binley (2011), Reducing monitoring gaps at the aquifer–river interface by modelling groundwater–surface water exchange flow patterns, *Hydrol. Processes*, *25*, 3547–3562, doi:10.1002/hyp.8080.

Naranjo, R. C., G. Pohll, R. G. Niswonger, M. Stone, and A. McKay (2013), Using heat as a tracer to estimate spatially distributed mean residence times in the hyporheic zone of a riffle-pool sequence, *Water Resour. Res.*, *49*, 3697–3711, doi:10.1002/wrcr.20306.

O'Connor, B. L., and J. W. Harvey (2008), Scaling hyporheic exchange and its influence on biogeochemical reactions in aquatic ecosystems, *Water Resour. Res.*, *44*, W12423, doi:10.1029/2008WR007160.

Packman, A., A. Marion, M. Zaramella, C. Chen, J.-F. Gaillard, and D. Keane (2006), Development of layered sediment structure and its effects on pore water transport and hyporheic exchange, *Water Air Soil Pollut.*, *6*(5), 433–442, doi:10.1007/s11267-006-9057-y.

Rosenberry, D., and J. Pitlick (2009), Local-scale spatial and temporal variability of seepage in a shallow gravel-bed river, *Hydrol. Processes*, *23*, 3306–3318.

Salehin, M., A. I. Packman, and M. Paradis (2004), Hyporheic exchange with heterogeneous streambeds: Laboratory experiments and modeling, *Water Resour. Res.*, *40*, W11504, doi:10.1029/2003WR002567.

Sawyer, A. H., and M. B. Cardenas (2009), Hyporheic flow and residence time distributions in heterogeneous cross-bedded sediment, *Water Resour. Res.*, *45*, W08406, doi:10.1029/2008WR007632.

Sawyer, A. H., M. B. Cardenas, and J. Buttles (2011), Hyporheic exchange due to channel-spanning logs, *Water Resour. Res.*, *47*, W08502, doi:10.1029/2011WR010484.

Sawyer, A. H., M. B. Cardenas, and J. Buttles (2012), Hyporheic temperature dynamics and heat exchange near channel-spanning logs, *Water Resour. Res.*, *48*, W01529, doi:10.1029/2011WR011200.

Sophocleous, M. (2002), Interactions between groundwater and surface water: the state of the science, *Hydrogeol. J.*, *10*(1), 52–67, doi:10.1007/s10040-001-0170-8.

Stonedahl, S. H., J. W. Harvey, A. Wörman, M. Salehin, and A. I. Packman (2010), A multiscale model for integrating hyporheic exchange from ripples to meanders, *Water Resour. Res.*, *46*, W12539, doi:10.1029/2009WR008865.

Storey, R. G., K. W. F. Howard, and D. D. Williams (2003), Factors controlling riffle-scale hyporheic exchange flows and their seasonal changes in a gaining stream: A three-dimensional groundwater flow model, *Water Resour. Res.*, *39*(2), 1034, doi:10.1029/2002WR001367.

Thibodeaux, L. J., and J. D. Boyle (1987), Bedform-generated convective transport in bottom sediments, *Nature*, *325*, 341–343.

Tonina, D., and J. M. Buffington (2007), Hyporheic exchange in gravel bed rivers with pool-riffle morphology: Laboratory experiments and three-dimensional modeling, *Water Resour. Res.*, *43*, W01421, doi:10.1029/2005WR004328.

Tonina, D., and J. M. Buffington (2009), Hyporheic exchange in mountain rivers. I: Mechanics and environmental effects, *Geogr. Compass*, *3*(3), 1038–1062, doi:10.1111/j.1749-8198.2009.00226.x.

Tonina, D., and J. M. Buffington (2011), Effects of stream discharge, alluvial depth and bar amplitude on hyporheic flow in pool-riffle channels, *Water Resour. Res.*, *47*, W08508, doi:10.1029/2010WR009140.

Triska, F. J., V. C. Kennedy, R. J. Avanzino, G. W. Zellweger, and K. E. Bencala (1989), Retention and transport of nutrients in a third-order stream in northwest California: Hyporheic processes, *Ecology*, *70*(6), 1893–1905.

Varni, M., and J. Carrera (1998), Simulation of groundwater age distributions, *Water Resour. Res.*, *34*(12), 3271–3281.

Ward, A. S., M. N. Gooseff, and P. A. Johnson (2011), How can subsurface modifications to hydraulic conductivity be designed as stream restoration structures? Analysis of Vaux's conceptual models to enhance hyporheic exchange, *Water Resour. Res.*, *47*, W08512, doi:10.1029/2010WR010028.

Ward, A. S., M. N. Gooseff, and K. Singha (2012), How does subsurface characterization affect prediction of hyporheic exchange?, *Ground Water*, *51*(1), 14–28, doi:10.1111/j.1745–6584.2012.00911.x.

Wörman, A., A. Packman, L. Marklund, J. Harvey, and S. Stone (2007), Fractal topography and subsurface water flows from fluvial bedforms to the continental shield, *Geophys. Res. Lett.*, *34*, L07402, doi:10.1029/2007GL029426.

Xu, M., and Y. Eckstein (1997), Statistical analysis of the relationships between dispersivity and other physical properties of porous media, *Hydrogeol. J.*, *5*(4), 4–20.

Zarnetske, J. P., R. Haggerty, S. M. Wondzell, and M. A. Baker (2011a), Dynamics of nitrate production and removal as a function of residence time in the hyporheic zone, *J. Geophys. Res.*, *116*, G01025, doi:10.1029/2010JG001356.

Zarnetske, J. P., R. Haggerty, S. M. Wondzell, and M. A. Baker (2011b), Labile dissolved organic carbon supply limits hyporheic denitrification, *J. Geophys. Res.*, *116*, G04036, doi:10.1029/2011JG001730.

Zarnetske, J. P., R. Haggerty, S. M. Wondzell, V. A. Bokil, and R. Gonzalez-Pinzon (2012), Coupled transport and reaction kinetics control the nitrate source-sink function of hyporheic zones, *Water Resour. Res.*, *48*, W11508, doi:10.1029/2012WR011894.

Zlotnik, V. A., M. B. Cardenas, and D. Toundykov (2010), Effects of multiscale anisotropy on basin and hyporheic groundwater flow, *Ground Water*, *49*(4), 576–583, doi:10.1111/j.1745–6584.2010.00775.x.

